

# Structural and functional properties of the transporter SLC26A6 reveal mechanism of coupled anion exchange

David N Tippett<sup>1</sup>, Colum Breen<sup>2</sup>, Stephen J Butler<sup>2</sup>, Marta Sawicka<sup>1</sup>, Raimund Dutzler<sup>1\*</sup>

<sup>1</sup>Department of Biochemistry, University of Zurich, Zurich, Switzerland; <sup>2</sup>Department of Chemistry, Loughborough University, Loughborough, United Kingdom

**Abstract** Members of the SLC26 family constitute a conserved class of anion transport proteins, which encompasses uncoupled transporters with channel-like properties, coupled exchangers and motor proteins. Among the 10 functional paralogs in humans, several participate in the secretion of bicarbonate in exchange with chloride and thus play an important role in maintaining pH homeostasis. Previously, we have elucidated the structure of murine SLC26A9 and defined its function as an uncoupled chloride transporter (Walter et al., 2019). Here we have determined the structure of the closely related human transporter SLC26A6 and characterized it as a coupled exchanger of chloride with bicarbonate and presumably also oxalate. The structure defines an inward-facing conformation of the protein that generally resembles known structures of SLC26A9. The altered anion selectivity between both paralogs is a consequence of a remodeled ion binding site located in the center of a mobile unit of the membrane-inserted domain, which also accounts for differences in the coupling mechanism.

\*For correspondence: dutzler@bioc.uzh.ch

**Competing interest:** The authors declare that no competing interests exist.

**Funding:** See page 22

**Preprint posted**  
06 March 2023

**Sent for Review**  
06 March 2023

**Reviewed preprint posted**  
14 April 2023

**Reviewed preprint revised**  
19 May 2023

**Version of Record published**  
23 June 2023

**Reviewing Editor:** Randy B Stockbridge, University of Michigan, United States

© Copyright Tippett et al. This article is distributed under the terms of the [Creative Commons Attribution License](https://creativecommons.org/licenses/by/4.0/), which permits unrestricted use and redistribution provided that the original author and source are credited.

## eLife assessment

This **important** manuscript combines cryo-EM and a suite of **compelling** whole cell and proteoliposome transport assays to establish the mechanism and structure of the full-length human SLC26A6 chloride/bicarbonate exchangers, including the first partial view of the previously unresolved IVS region of an SLC26 STAS domain. In combination with prior studies on additional SLC26 paralogs, including the SLC26A9 paralog initially reported by the same group, the study provides broadly relevant insights into the mechanistic diversity of the SLC26 transporters. This study is of interest to the biophysics community and the field of membrane transport.

## Introduction

Bicarbonate ( $\text{HCO}_3^-$ ), the conjugate base of carbonic acid, is a waste product of the citric acid cycle and an important buffer in the intra- and extracellular environment. Its transport across cellular membranes thus constitutes an important mechanism for the control of intracellular pH and the increase of the buffer capacity of bodily fluids and secretions (**Alka and Casey, 2014**). This process is mediated by distinct channels and secondary transporters, the latter comprising paralogs of the SLC4 and SLC26 families. The SLC26 transporters constitute an abundant class of anion transport proteins that are expressed in all kingdoms of life with a considerable degree of sequence conservation (**Alper and Sharma, 2013; Dorwart et al., 2008**). Homologs in prokaryotes and plants were classified as symporters, where the uptake of mono- and divalent anions is coupled to the import of either sodium ions or protons (**Geertsma et al., 2015; Wang et al., 2019; Wang et al., 2021**). However,

the transporters in animals show mechanistic differences. Among the 10 functional SLC26 paralogs in humans, we find an astonishing mechanistic breadth. Family members function as either coupled anion exchangers, anion transporters with channel-like properties and in the case of SLC26A5 (Prestin), as a motor protein in cochlear outer hair cells (*Alper and Sharma, 2013*). Among the paralogs which have retained their transport function, the distinction between coupled and uncoupled transporters is most pronounced. Whereas most family members operate as exchangers of different anions including the monovalent ions chloride ( $\text{Cl}^-$ ),  $\text{HCO}_3^-$ , iodide ( $\text{I}^-$ ) and formate and the divalent ions sulfate and oxalate (*Alper and Sharma, 2013*), the protein SLC26A9 functions as fast passive transporter of  $\text{Cl}^-$  (*Dorwart et al., 2007; Walter et al., 2019*). Our previous study has characterized the structural and functional properties of the murine ortholog of SLC26A9 (*Walter et al., 2019*). The protein adopts a homodimeric architecture that is representative for the entire SLC26 family. Each subunit consists of a membrane-inserted transport domain (TM) followed by a cytoplasmic STAS domain, which together with the extended N-terminus mediates the bulk of the subunit interactions with few contacts in the membrane-inserted region (*Walter et al., 2019*). The TMs share a protein fold that was initially identified in the prokaryotic transporter UraA (*Lu et al., 2011*), and that was later defined in the prokaryotic homologue SLC26Dg as common architecture for the entire family (*Geertsma et al., 2015*). In this architecture, the TM segregates into two separate motifs that adopt distinct roles during transport, respectively termed 'core' and 'gate' domains. The gate domain forms a contiguous rigid scaffold with the cytosolic STAS domain that remains static during transport. Conversely the mobile core domain harbors a selective anion binding site and acts as mobile unit during transport. This unit alternately exposes the substrate site to different sides of the membrane as expected for a protein working by an elevator-type transport mechanism (*Drew and Boudker, 2016; Walter et al., 2019*). Despite its classification as membrane transporter, SLC26A9 mediates large channel-like chloride currents that saturate at high mM concentration and it efficiently discriminates against  $\text{HCO}_3^-$  (*Dorwart et al., 2007; Walter et al., 2019*). Its function as a fast electrogenic chloride transporter and selection against  $\text{HCO}_3^-$  is astonishing since several other family members have been classified as  $\text{Cl}^-/\text{HCO}_3^-$  exchangers (*Alper and Sharma, 2013*). One of the family members sharing this property is the protein SLC26A6 (*Knauf et al., 2001; Lohi et al., 2000*). SLC26A6 is widely expressed in different tissues including the heart, kidney, pancreas, and intestine (*Wang et al., 2020*). Besides its function as a  $\text{HCO}_3^-$  transporter, it also plays an important role in the extrusion of oxalate to prevent the formation of kidney stones (*Clark et al., 2008; Jiang et al., 2006; Ohana et al., 2013*). Similar to SLC26A9, the protein acts in synergy with the chloride channel CFTR and was proposed to engage in direct interaction and mutual regulation (*Bertrand et al., 2017; Dorwart et al., 2008; Shcheynikov et al., 2006a; Wang et al., 2006*). The stoichiometry of  $\text{HCO}_3^-$  and oxalate transport by SLC26 is still controversial, as transport of both ions has been described in different studies as either electrogenic or electroneutral (*Chernova et al., 2005; Clark et al., 2008; Kim et al., 2013; Ohana et al., 2009; Shcheynikov et al., 2006b; Xie et al., 2002*). This question is particularly pertinent in light of the divergent net charge of both substrates, with  $\text{HCO}_3^-$  being monovalent and oxalate divalent under physiological conditions. Consequently, the structural basis for the mechanistic distinction between the uncoupled SLC26A9 and the coupled SLC26A6 and the basis for their pronounced selectivity, with  $\text{Cl}^-$  acting as common substrate of both proteins, has remained elusive.

To address these open questions, we here present a thorough structural and functional characterization of the human transporter SLC26A6 combining cryo-electron microscopy with electrophysiology and liposomal transport assays. With respect to its overall structure, SLC26A6 closely resembles its paralog SLC26A9, although it shows a distinct transport mechanism. The protein mediates electro-neutral  $\text{Cl}^-/\text{HCO}_3^-$  and presumable electrogenic  $\text{Cl}^-/\text{oxalate}$  exchange, which is in stark contrast to the uncoupled  $\text{Cl}^-$  transport of SLC26A9. This is accomplished by an altered ion binding site located in the mobile core domain of the transmembrane transport unit.

## Results

### Functional characterization of SLC26A6

We have previously characterized the transport properties of murine SLC26A9 by patch clamp electrophysiology and found comparatively large and selective  $\text{Cl}^-$  currents. SLC26A9 currents were shown to reverse at the Nernst potential of the conducting anion, which distinguishes the protein as an

uncoupled chloride transporter (Walter et al., 2019; Figure 1A, Figure 1—figure supplement 1A). The high magnitude of these ohmic currents, which lack any time-dependence in response to voltage changes, originate from an unusually active protein that transports anions with channel-like properties (Figure 1—figure supplement 1A). SLC26A9 shows a lyotropic permeability sequence that facilitates the transport of Cl<sup>-</sup>, isothiocyanate, I<sup>-</sup> and nitrate but not sulfate or HCO<sub>3</sub><sup>-</sup> (Walter et al., 2019; Figure 1A, Figure 1—figure supplement 1A). The inability to conduct HCO<sub>3</sub><sup>-</sup> is an exception in a family where most members work as transporters of this abundant anion (Alper and Sharma, 2013; Ohana et al., 2009). To investigate mechanistic differences between this passive Cl<sup>-</sup> transporter and its paralogs functioning as coupled antiporters, we have turned our attention towards the protein SLC26A6, which was proposed to mediate electrogenic Cl<sup>-</sup>/HCO<sub>3</sub><sup>-</sup> exchange (Ohana et al., 2009; Shcheynikov et al., 2006b). Hence, we initially attempted to use patch clamp electrophysiology in the whole-cell configuration to characterize its transport properties. However, unlike for SLC26A9, we did not detect specific currents that could be attributed to SLC26A6 in a wide voltage range. This was irrespective of whether we used symmetric Cl<sup>-</sup> solutions or asymmetric conditions, where the major anion in the extracellular solution was changed to HCO<sub>3</sub><sup>-</sup> (Figure 1B, Figure 1—figure supplement 1B). To confirm the expression of SLC26A6 at the plasma membrane, we employed surface biotinylation and found a similar level as observed for its electrogenic paralog SLC26A9 (Figure 1C). We thus concluded that the transporter would either be inactive, exceedingly slow or that transport would be electroneutral as a consequence of the strict 1:1 exchange of two monovalent anions.

Consequently, we turned to in vitro assays where we have reconstituted SLC26A6 into proteoliposomes and monitored its activity with ion-selective probes (Figure 1—figure supplement 1C). Initially, we investigated whether we would be able to detect any sign of uncoupled chloride flow by using a fluorometric assay based on the fluorophore ACMA. This assay monitors pH changes following the ionophore-mediated H<sup>+</sup> influx to compensate for the buildup of a membrane potential during Cl<sup>-</sup> uptake, which would enable us to observe transport even if the slow kinetics prevents characterization by electrophysiology (Figure 1—figure supplement 1C). In this way, we have previously monitored SLC26A9-mediated anion transport into proteoliposomes (Walter et al., 2019). However, in contrast to SLC26A9, no acidification was observed for SLC26A6, emphasizing that the transporter is either inactive or, alternatively, transport would be strictly coupled and electroneutral (Figure 1D).

Next, we were interested in whether Cl<sup>-</sup> would be exchanged by HCO<sub>3</sub><sup>-</sup> by a mechanism where the charges of transported anions are balanced. To this end, we directly monitored Cl<sup>-</sup> influx into HCO<sub>3</sub><sup>-</sup>-loaded proteoliposomes using the fluorophore lucigenin, whose fluorescence is selectively quenched by the former anion (Figure 1—figure supplement 1C). In this assay, we found a robust time-dependent fluorescence decrease at high Cl<sup>-</sup> concentration, demonstrating its transport by SLC26A6 (Figure 1E, Figure 1—figure supplement 1D, E). The process did not require the addition of valinomycin to dissipate the membrane potential, thus underlining that transport is electroneutral. In the investigation of the Cl<sup>-</sup> concentration-dependence of transport, we found a saturation with an apparent K<sub>M</sub> of about 16–37 mM (Figure 1F, Figure 1—figure supplement 1F). This indicated low affinity for the transported anion is in the same range as observed for Cl<sup>-</sup> transport in SLC26A9 (Walter et al., 2019).

Finally, we probed whether HCO<sub>3</sub><sup>-</sup> itself would be a transported substrate. To this end, we employed a novel HCO<sub>3</sub><sup>-</sup>-selective europium probe and incorporated this probe within proteoliposomes to assay HCO<sub>3</sub><sup>-</sup> influx (Figure 1—figure supplement 1C; Martínez-Crespo et al., 2021). The addition of 10 mM HCO<sub>3</sub><sup>-</sup> to the outside in presence of a symmetric 200 mM concentration of Cl<sup>-</sup> on both sides of the membrane caused a pronounced increase in luminescence that is well above the small non-specific signal observed in liposomes not containing any protein (Figure 1G). This increase is substantially enhanced when using a reduced outside Cl<sup>-</sup> concentration of 50 mM to generate an outwardly directed driving force (Figure 1G). Together these experiments demonstrate that HCO<sub>3</sub><sup>-</sup> is a transported anion and that its import into proteoliposomes is coupled to the counterflow of Cl<sup>-</sup>. Taken together, our experiments underline the function of SLC26A6 as electroneutral coupled Cl<sup>-</sup>/HCO<sub>3</sub><sup>-</sup> exchanger.

Besides HCO<sub>3</sub><sup>-</sup>, SLC26A6 was also proposed to be involved in the transport of oxalate in exchange for Cl<sup>-</sup> and thus to participate in the excretion of this small divalent anion in both the intestine and kidneys (Clark et al., 2008; Ohana et al., 2013). However, if assuming a coupled 1:1 stoichiometry as observed in case of Cl<sup>-</sup>/HCO<sub>3</sub><sup>-</sup> exchange, the transported charge would in this case no longer be

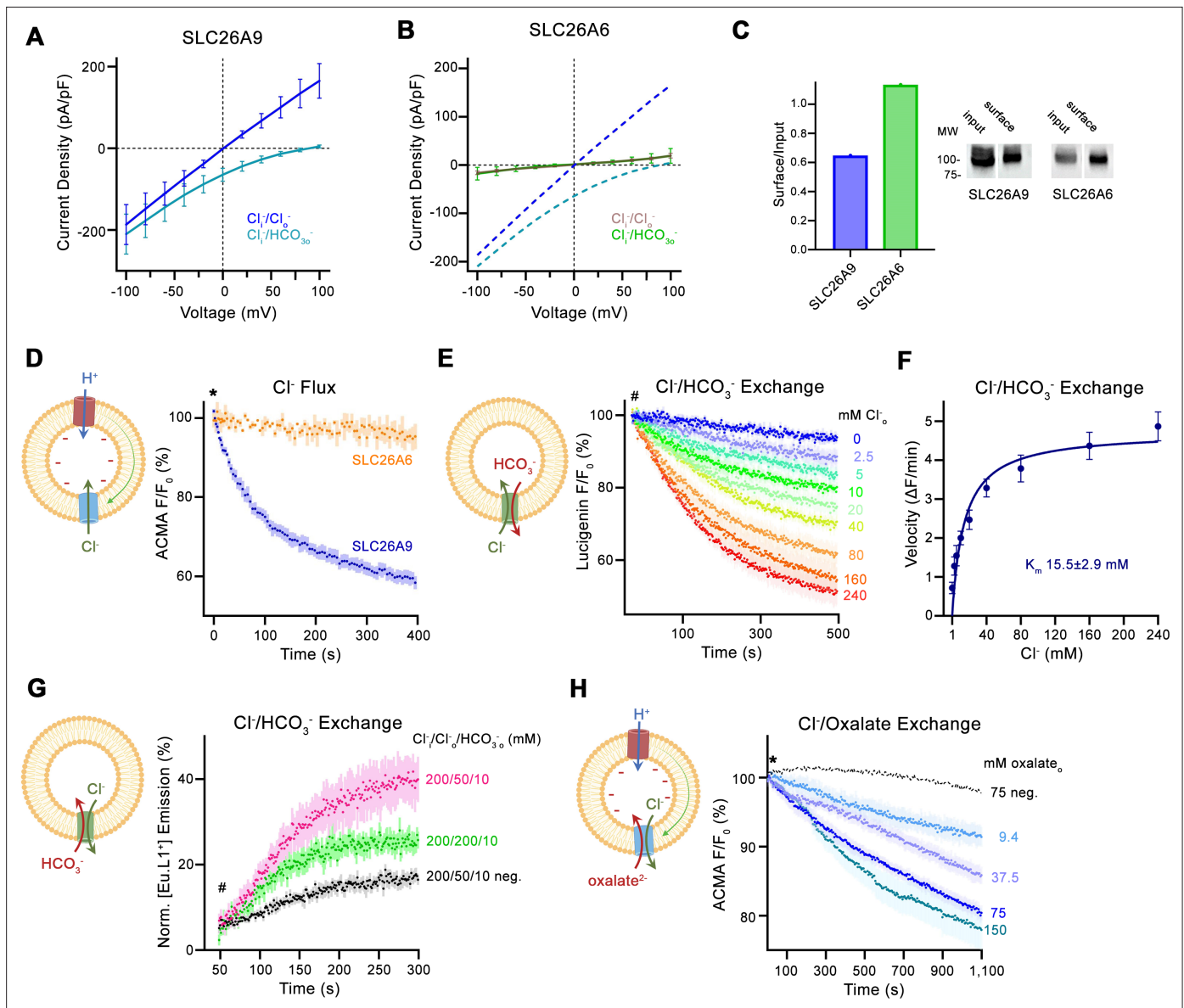


**Figure 1.** Transport properties of SLC26A6. **(A)** Current-Voltage relationships of HEK 293 cells expressing murine SLC26A9 and **(B)** human SLC26A6. Data were recorded in the whole-cell configuration in symmetric (150 mM) Cl<sup>-</sup> concentrations and asymmetric conditions with equimolar (150 mM) concentrations of intracellular Cl<sup>-</sup> and extracellular HCO<sub>3</sub><sup>-</sup>. Values show mean of independent experiments (SLC26A9 Cl<sup>-</sup>/Cl<sup>-</sup> n=6, Cl<sup>-</sup>/HCO<sub>3</sub><sup>-</sup> n=6; SLC26A6 Cl<sup>-</sup>/Cl<sup>-</sup> n=6, Cl<sup>-</sup>/HCO<sub>3</sub><sup>-</sup> n=6). Dashed lines in **(B)** correspond to SLC26A9 data displayed in **(A)**. **(C)** Protein expression at the surface of HEK cells determined by surface biotinylation. Ratio of biotinylated (right) over total protein (left) as quantified from a Western blot against a myc-tag fused to the C-terminus of the respective constructs. **(D)** Uncoupled Cl<sup>-</sup> transport mediated by either the modified murine construct SLC26A9<sup>T</sup> or SLC26A6 reconstituted into proteoliposomes, as monitored by the fluorescence change of the pH gradient-sensitive fluorophore ACMA. Traces show mean of seven and three replicates from two independent reconstitutions for SLC26A9<sup>T</sup> and SLC26A6. **(E)** Coupled Cl<sup>-</sup>/HCO<sub>3</sub><sup>-</sup> exchange monitored by the time- and concentration-dependent quenching of the fluorophore luciferin trapped inside proteoliposomes containing SLC26A6. Traces show mean of six independent experiments from two reconstitutions. **(F)** Cl<sup>-</sup> concentration dependence of transport. Initial velocities were obtained from individual measurements displayed in **(E)**, the solid line shows a fit to the Michaelis Menten equation with an apparent K<sub>m</sub> of 16 mM. **(G)** Coupled Cl<sup>-</sup>/HCO<sub>3</sub><sup>-</sup> exchange monitored by the time- and concentration-dependent luminescence increase of the HCO<sub>3</sub><sup>-</sup>-selective probe [Eu.L1<sup>+</sup>] trapped inside proteoliposomes containing SLC26A6. Traces show mean of five independent experiments from three reconstitutions. 'neg.' refers to mock liposomes. **(E, G)**, Hashtag indicates addition of the assayed anion. **(H)** Electrogenic oxalate uptake followed by the fluorescence change of the pH gradient sensitive fluorophore ACMA. Traces show mean quenching of ACMA fluorescence in a time- and concentration-dependent manner for SLC26A6 proteoliposomes with outside oxalate concentrations of 9.4 mM (n=3), 37.5 mM (n=5), 75 mM (n=6), 150 mM (n=8, all from two independent reconstitutions). Neg. refers to mock liposomes assayed upon addition of 75 mM oxalate as defined in **Figure 1—figure supplement**

Figure 1 continued on next page



Figure 1 continued

**1G** (D, H), Asterisk indicates addition of the H<sup>+</sup> ionophore CCCP, which allows counterion movement and electrogenic Cl<sup>-</sup> transport to proceed. (A, B, D–H), errors are s.e.m. (D, E, G, H) Scheme of the respective assay is shown left.

The online version of this article includes the following source data and figure supplement(s) for figure 1:

**Source data 1.** Electrophysiology, liposomal transport assay data and western blot.

**Figure supplement 1.** Transport data.

**Figure supplement 1—source data 1.** Extended electrophysiology and liposomal transport assay data.

balanced, thus converting an electroneutral into an electrogenic transport process. As there are no suitable fluorophores for the selective detection of oxalate and since the small dicarboxylic acid also interferes with the detection of Cl<sup>-</sup> by lucigenin, we decided to investigate whether a potentially electrogenic Cl<sup>-</sup>/oxalate exchange could be assayed with the fluorophore ACMA (**Figure 1—figure supplement 1C**). In these experiments, we found a robust decrease of the ACMA fluorescence upon the addition of extracellular oxalate to Cl<sup>-</sup>-loaded proteoliposomes containing SLC26A6, with the concentration dependence and saturation of the fluorescence decay further emphasizing a specific transport process (**Figure 1H**). We also attempted to follow electrogenic Cl<sup>-</sup>/oxalate exchange by patch clamp electrophysiology in the whole cell configuration but did not measure pronounced currents that would be above background, likely due to the slow kinetics of the process (**Figure 1—figure supplement 1I**). Together, our functional experiments characterize SLC26A6 as a strictly coupled transporter that exchanges Cl<sup>-</sup> with HCO<sub>3</sub><sup>-</sup> and presumably also oxalate at a 1:1 stoichiometric ratio.

### SLC26A6 structure

To reveal the molecular basis of the described transport properties of SLC26A6, we have determined its structure by cryo-electron microscopy (cryo-EM). A dataset of the protein purified in the detergent glycol-diosgenin (GDN) at 3.3 Å was of high quality and allowed for the unambiguous interpretation of the cryo-EM density by an atomic model (**Figure 2A, Figure 2—figure supplements 1 and 2, Table 1**). In its organization, the SLC26A6 structure shows familiar features that have previously been observed in various eukaryotic family members of known structure including human and murine SLC26A9 (**Chi et al., 2020; Walter et al., 2019**), SLC26A5 (**Bavi et al., 2021; Butan et al., 2022; Futamata et al., 2022; Ge et al., 2021**), SLC26A4 (**Liu et al., 2023**) and the plant transporter AtSULTR4 (**Wang et al., 2021; Figure 2B, Figure 2—figure supplement 3**). The SLC26A6 subunit consists of a membrane-inserted unit (TM) followed by a cytoplasmic STAS domain. In the homodimeric protein, subunit interactions are predominantly formed by the domain-swapped cytoplasmic parts including an extended N-terminal region and the C-terminal STAS domain, whereas the few contacts between the transmembrane transport units are confined to the end of the terminal membrane-spanning helix  $\alpha$ 14 (**Figure 2B**). A region connecting secondary structure elements of the STAS domain (located between C $\alpha$ 1 and  $\beta$ 4) termed the intervening sequence (IVS) is present in the characterized protein (**Figure 2C**). Previously, removal of this region increased both the stability and surface expression of a construct of the murine SLC26A9 while retaining its transport properties (**Walter et al., 2019**). In the density, the N-terminal part of the IVS folds into an  $\alpha$ -helix encompassing amino acids 569–593 (C $\alpha$ <sup>IVS</sup>) whereas the following 61 residues are unstructured and thus not resolved in the density (**Figure 2A**). On the C-terminus of the IVS, the density re-appears at Ser 655 at the region preceding  $\beta$ 4, which interacts with C $\alpha$ <sup>IVS</sup> (**Figure 2B and C**). A generally similar arrangement was also observed in a full-length construct of human SLC26A9 (**Chi et al., 2020; Figure 2D**). In both structures, C $\alpha$ <sup>IVS</sup> runs about parallel to the membrane plane and contacts the loop connecting  $\alpha$ 8 and  $\alpha$ 9 of the mobile core domain. This presumably influences its conformational preferences thereby potentially impacting transport (**Figure 2B–D**).

### The transmembrane domain

In the dimeric transporter, the two TMs share minimal contacts and thus supposedly function as independent units (**Figure 2B**). Consequently, we expect structural differences underlying the distinct transport properties of SLC26 paralogs to be manifested in this part of the protein. Like in other pro- and eukaryotic family members of known structure, the TMs of SLC26A6 consist of two topologically related repeats of seven transmembrane segments, which span the membrane with opposite

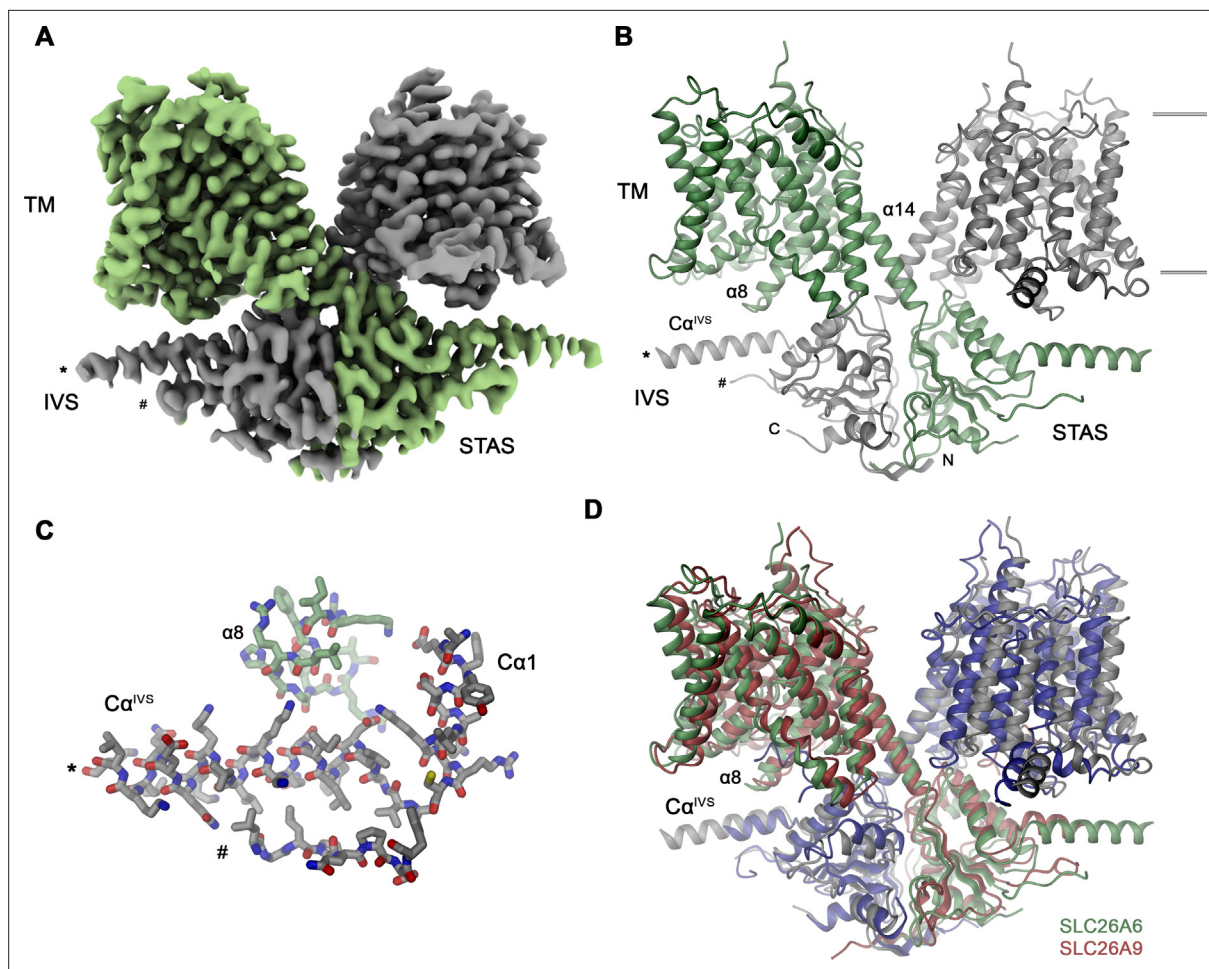


**Figure 2.** SLC26A6 structure. **(A)** Cryo-EM density of the SLC26A6 dimer at 3.28 Å and **(B)** ribbon representation of the model in the same orientation. Subunits are shown in unique colors and selected structural elements are labeled. The membrane boundary is indicated. **(C)** Interaction region between the loop preceding  $\alpha 8$  of the core domain and the helix  $\text{Ca}^{\text{IVS}}$  of the adjacent subunit. **(A–C)** Start (\*) and end (#) of the disordered region of the IVS are indicated. **(D)** Ribbon representation of the superimposed SLC26A6 (green, gray) and SLC26A9 (red, blue, PDBID: 7CH1) dimers.

The online version of this article includes the following figure supplement(s) for figure 2:

**Figure supplement 1.** Cryo-EM reconstruction of SLC26A6.

**Figure supplement 2.** Section of the cryo-EM density of SLC26A6.

**Figure supplement 3.** Sequence and Topology.

orientation (**Figure 2—figure supplement 3B**). Elements of both repeats are intertwined to form two segregated modules, a gate domain and a core domain (**Figure 3A**). The equivalence between the SLC26A6 and SLC26A9 conformations is illustrated in the overlay of the respective TMs whose  $\text{Ca}$  positions superimpose with an RMSD of 1.3 Å (**Figure 3B**). Both conformations represent inward-facing states of transporters presumably functioning by an alternate access mechanism. The substrate binding site located in the center of the core domain is accessible from the cytoplasm via a spacious aqueous cavity, whereas the extracellular exit is sealed by extended contacts between core and gate domains (**Figure 3C and D, Figure 3—figure supplement 1A, B**). The resemblance between individual sub-domains even exceeds the overall similarity of the TM (with core- and gate domains superimposing with RMSDs of 1.13 Å and 1.2 Å, respectively) distinguishing them as largely independent units of a modular protein (**Figure 3B**). In the comparison of both paralogs, the gate domains do not show pronounced differences (**Figure 3B**). Together with the cytoplasmic STAS domains, which constitute the bulk of the dimer interface, these sub-domains form a contiguous rigid scaffold of the dimeric protein that presumably remains static during transport (**Figure 2B, Figure 3—figure supplement 1C**). In contrast, both core domains represent the mobile elements of the protein (**Figure 3—figure**

**Table 1.** Cryo-EM data collection, refinement, and validation statistics.

	hSLC26A6 in GDN (EMDB-17085) (PDB 8OPQ)	
Data collection and processing	Data Set 1	Data Set 2
Magnification	130,000	130,000
Voltage (kV)	300	300
Electron exposure (e <sup>-</sup> /Å <sup>2</sup> )	61	67
Defocus range (μm)	-0.8 to -2.4	-1 to -2.4
Pixel size (Å) <sup>*</sup>	0.3255 (0.651)	0.3255 (0.651)
Symmetry imposed	C2	
Initial particle images (no.)	1,749,907	
Final particle images (no.)	93,169	
Map resolution (Å) FSC threshold 0.143	3.28	
Map resolution range (Å)	2.9–4.1	
<b>Refinement</b>		
Model resolution (Å) 0.5 FSC Threshold	3.3	
Model resolution range (Å)	1.6–3.3	
Map sharpening b-factor (Å <sup>2</sup> )	121.9	
Model composition		
Non-hydrogen atoms	10,006	
Protein residues	1296	
Ligands	2	
B factors (Å <sup>2</sup> )		
Protein	58.64	
Ligands	30	
R.m.s. deviations		
Bond lengths (Å)	0.004	
Bond angles (°)	0.907	
Validation		
MolProbity score	1.71	
Clashscore	8.25	
Poor rotamers (%)	0	
Ramachandran plot		
Favored (%)	96.18	
Allowed (%)	3.82	
Disallowed (%)	0.0	

1. \*Values in parentheses indicate the pixel size in super-resolution.

**supplement 1D**). Each core domain carries a substrate binding site located in a pocket at the center of the unit facing the gate domain (**Figures 3C, D , and 4A**). The presumable location of a bound chloride ion is resolved in the structure of SLC26A6 at a low contour of the map (**Figure 4B, Figure 2—figure supplement 2B**). This position concurs with positions inferred from known structures of paralogs, which show binding of Cl<sup>-</sup> and HCO<sub>3</sub><sup>-</sup> to an equivalent location (**Chi et al., 2020; Futamata et al., 2022; Ge et al., 2021; Liu et al., 2023; Figure 4B, Figure 4—figure supplement 1**). The anion binding site is placed between the opposed short helices α3 and α10, which partly span the membrane and whose N-termini are aligned to face each other in the center of the core domain (**Figure 4A**). Together with the side chains of surrounding residues, both α-helix termini form a selective anion binding site (**Figure 4B–G, Figure 4—figure supplement 1**). In complex with its bound cargo, the core domain is believed to shuttle as rigid unit between two extreme conformations where

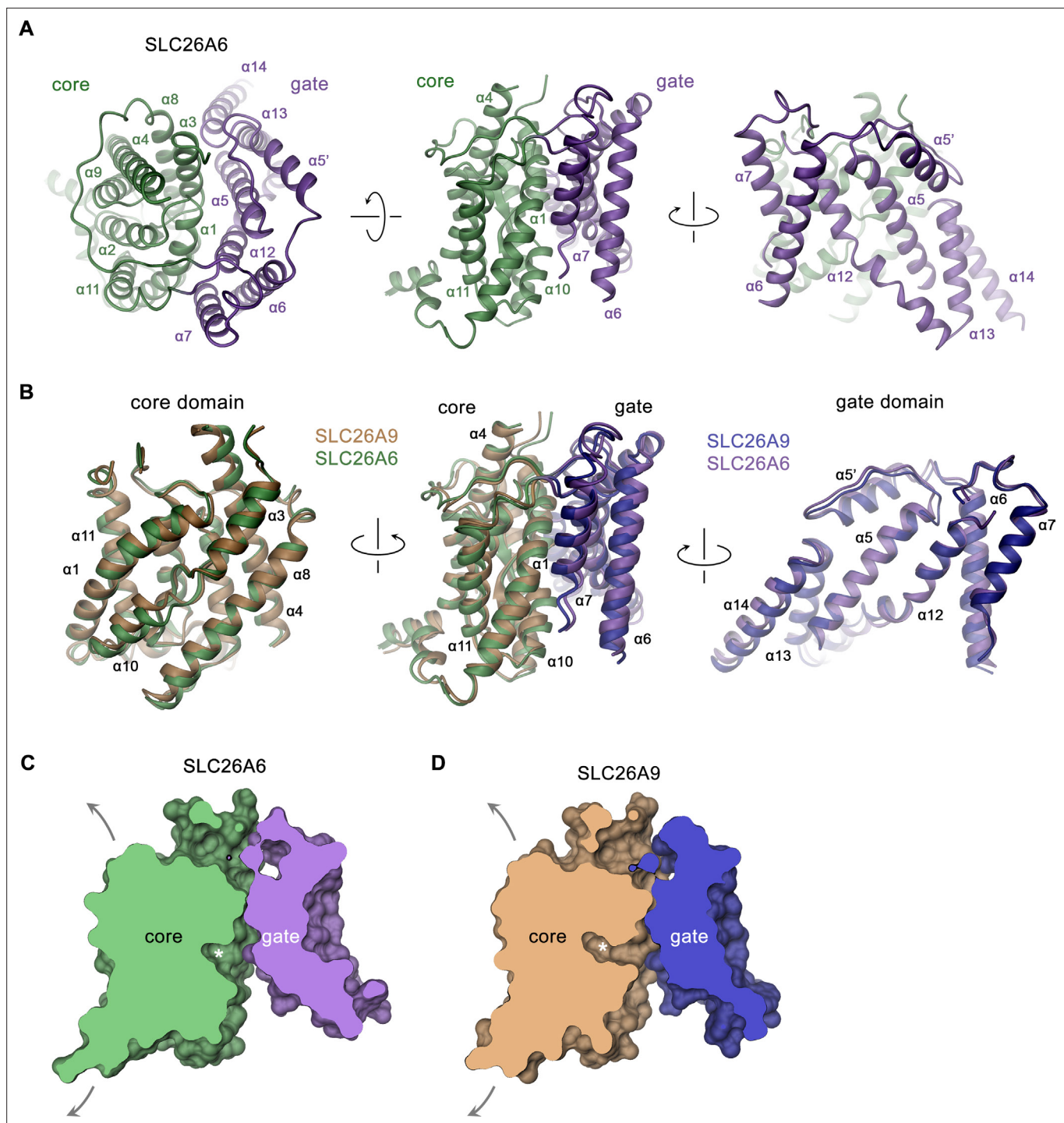


**Figure 3.** SLC26A6 TM domain. **(A)** Ribbon representation of the TM unit of SLC26A6 in indicated orientations (left, view is from the outside, center and right, from within the membrane). Core and gate domains are colored in green and violet, respectively. Selected secondary structure elements are labeled. **(B)** Superposition of elements of the TM between SLC26A6 and SLC26A9 (PDBID: 7CH1). Left, core domains, center, TMs, right, gate domains. Core and gate domains of SLC26A9 are colored in orange and blue, respectively. The view is from within the membrane with relative orientations indicated. **(C, D)** Slice across a surface of the TM domains of SLC26A6 **(C)** and SLC26A9 **(D)** viewed from within the membrane. The spacious aqueous cavity leading to the ion binding site from the cytoplasm is evident. Asterisk indicated the position of the transported ion. Arrows indicate possible movements of the core domain.

The online version of this article includes the following figure supplement(s) for figure 3:

**Figure supplement 1.** TM domain features.



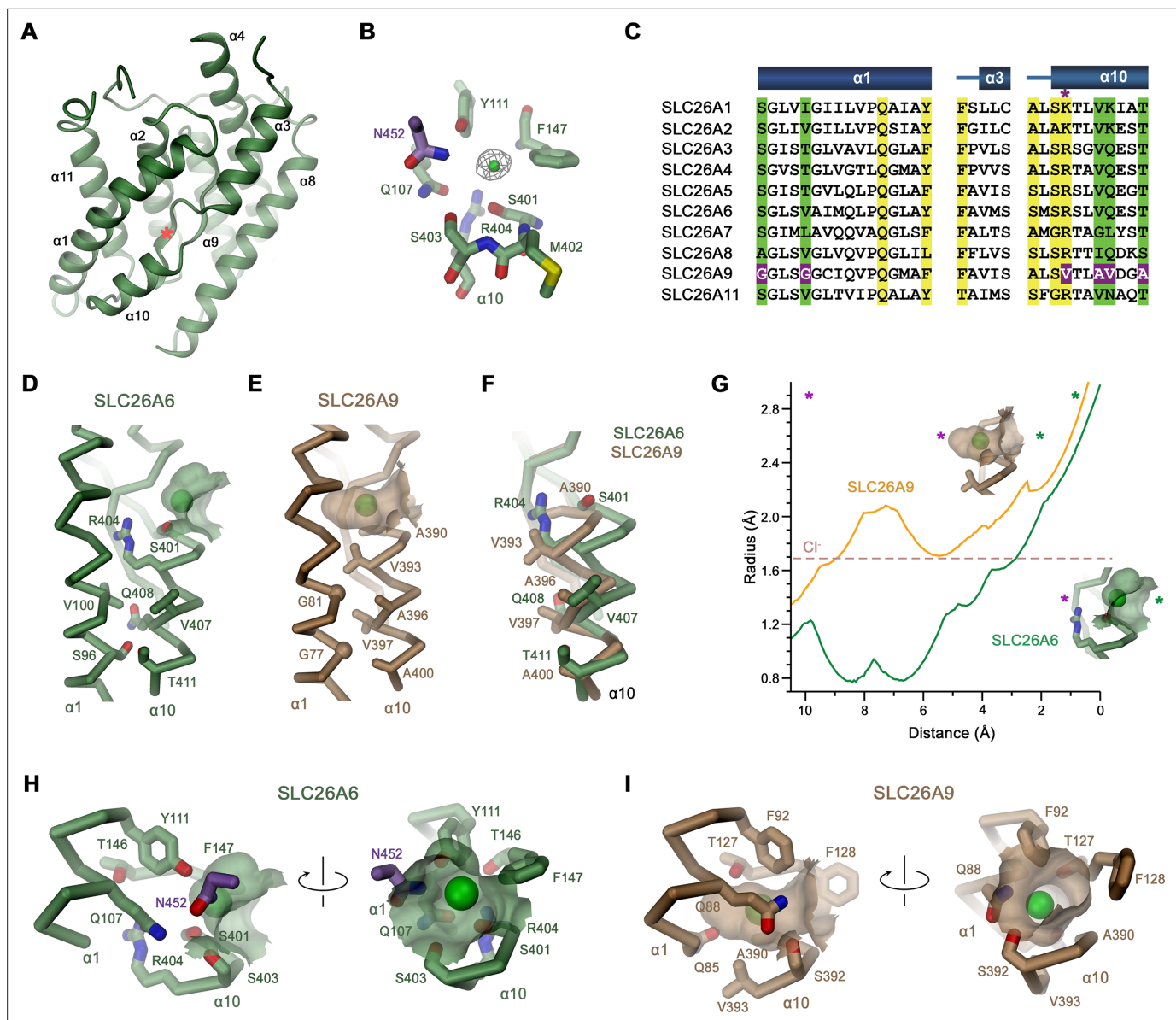


**Figure 4.** Features of the substrate binding site. **(A)** Ribbon representation of the core domain of SLC26A6 viewed from within the membrane from the gate domain. Asterisk indicates the location of the ion binding site, selected secondary structure elements are labeled. **(B)** Ion binding site with the density of a bound Cl<sup>-</sup> ion (green) displayed as mesh. **(C)** Sequence alignment of the region constituting the ion binding site of the ten functional human SLC26 paralogs. Conserved residues in the contact region between α1 and α10 are highlighted in green, residues involved in ion interactions in yellow. Deviating residues in SLC26A9 are highlighted in violet. Asterisk marks position that harbors a basic residue in all family members except for SLC26A9, where the residue is replaced by a valine. Whereas most paralogs, including the ones operating as HCO<sub>3</sub><sup>-</sup> exchangers, carry an arginine at this site, the sulfate transporters SLC26A1 and 2 contain a smaller lysine. Secondary structure elements are shown above. **(D, E)** Cα-representation of the contact region between α1 and α10 of **(D)** SLC26A6 and **(E)** SLC26A9 (PDBID: 7CH1). **(F)** α10 of both transporters obtained from a superposition of the core domains. **(D–F)** Side chains of residues of the contact region and selected residues of the binding site are shown as sticks. **(G)** Size of the substrate cavity of SLC26A6 and SLC26A9 as calculated with HOLE (Smart et al., 1996). The radius of the substrate cavity of either protein is mapped along a trajectory connecting a start position at the entrance of each cavity (distance 0 Å) and an end position located outside of the cavity in the protein region (distance 10 Å). Both points are defined by asterisks in insets showing the substrate cavities for either transporter and they are indicated in the graph (green, cavity entrance towards the aqueous vestibule; violet, protein region). **(H, I)** Ion binding sites of SLC26A6 **(H)** and SLC26A9 **(I)**. The relative orientation of views is indicated. **(D, E, H, I)** The position of bound ions was inferred as detailed in Figure 1. The molecular surface surrounding the bound ions is displayed. Side chains of interacting residues are shown as sticks.

The online version of this article includes the following figure supplement(s) for figure 4:

**Figure supplement 1.** Binding site comparisons.



the binding site is either exposed to the cytoplasm or the extracellular environment (**Figure 3C and D, Figure 3—figure supplement 1D**).

As carrier of the substrate binding site, the core domains presumably display the characteristic features accounting for the distinct functional properties of SLC26A6 and SLC26A9. Their conservation within the SLC26 family is illustrated in the comparison of the respective domains of SLC26A6 and SLC26A5 (Prestin; **Figure 4C, Figure 4—figure supplement 1A, C, D, E, G**). Latter belongs to a protein that, instead of transporting ions, confers electromotility and which in the best defined structure (PDBID: 7LGU) resides in a distinct conformation where the substrate binding site has become buried between core and gate domain (leading to an RMSD of 2.9 Å for the entire TMD; **Ge et al., 2021**). Despite the functional and conformational differences, the core domains of SLC26A5 and SLC26A6 superimpose with an RMSD of only 1.13 Å, illustrating their close structural resemblance (**Figure 4—figure supplement 1A, C**). Both proteins share similar ion binding properties that extends to Cl<sup>-</sup> and HCO<sub>3</sub><sup>-</sup>, latter of which is not a substrate of SLC26A9 (**Walter et al., 2019**). In contrast to the general similarity with SLC26A5, the comparison of the same units of SLC26A6 and SLC26A9 shows distinct features that likely underlie the differences in substrate selectivity and transport mechanism (**Figure 4—figure supplement 1B,C**). These are confined to the conformation of α10, which at its N-terminus forms direct interactions with transported ions, whereas the remainder of the domain is very similar (**Figure 4—figure supplement 1B,C**). The difference in the conformations of this short membrane-inserted helix can be approximated by a 12–14° rotation of SLC26A9 around an axis located at its C-terminal end towards α-helix 1 (**Figure 4F, Figure 4—figure supplement 1B,C**). The replacement of residues within the contact region of SLC26A9 in comparison to other family members acts to lower their side chain volume at the contact region between both helices (**Figure 4C–F**). These include Ser 96 and Val 100 on SLC26A6, which are both replaced by glycines at equivalent positions in SLC26A9 (i.e., Gly 77 and Gly 81) and a substitution of Val 407, Gln 408 and Thr 411 by Ala 396, Val 397 and Ala 400 (**Figure 4C–F**). In addition to the described substitutions, there are also differences in the side chains surrounding the ion binding site, which together determine the size and polarity of the substrate binding pocket (**Figure 4C**). These differences extend to Ser 401 of SLC26A6, which is replaced by an alanine in SLC26A9 (Ala 390), and most prominent, the large Arg 404 of SLC26A6, which is replaced by Val 393 in SLC26A9 (**Figure 4C-I, Figure 4—figure supplement 1D–G**). As a result, the pocket is considerably deeper in SLC26A9 compared SLC26A6, where it is delimited by the side chain of Arg 404 that interacts with the residues preceding α helix 3 to form the back side of the shallow binding site (**Figure 4D–I, Figure 4—figure supplement 1D–H**). In addition to its structural role, Arg 404 likely also contributes to the stabilization of bound anions by coulombic interactions, with its guanidium group potentially engaging in direct interactions with bicarbonate or oxalate. The altered geometry of the site leads to the binding of Cl<sup>-</sup> deeper in the pocket in case of SLC26A9 (**Figure 4D, E,G-I, Figure 4—figure supplement 1H**) and presumably explains why bicarbonate interacts with SLC26A6 but not SLC26A9.

## Structure-function relationships

Whereas our functional data has defined SLC26A6 as a coupled antiporter that exchanges Cl<sup>-</sup> with HCO<sub>3</sub><sup>-</sup> and presumably also oxalate with equimolar stoichiometry, its structure has revealed the architecture of a transport protein in an inward-facing conformation. The transport properties are presumably determined by the detailed organization of the mobile core domain. This protein module shows pronounced structural differences compared to the equivalent unit of the uncoupled transporter SLC26A9, resulting in a remodeled anion binding site, which in SLC26A6 is lined by a conserved basic residue (i.e. Arg 404) that is shared by most but not all mammalian paralogs (**Figure 4C, Figure 4—figure supplement 1G, Figure 5A**). We thus decided to mutate this position to the amino acid found in SLC26A9 and to characterize the transport properties of the SLC26A6 mutant R404V. This mutation is well-tolerated and does not interfere with protein integrity as judged by its expression level and biochemical properties. We initially investigated whether SLC26A6 R404V would conduct ions as a consequence of compromised coupling properties and thus studied the protein by patch-clamp electrophysiology. In whole-cell patch clamp experiments, we detected small currents in symmetric Cl<sup>-</sup> solutions, which are low compared to SLC26A9, despite the comparable expression of the mutant at the cell-surface (**Figure 5B–E**). Irrespective of their magnitude, which is not significantly higher than SLC26A6 WT (**Figure 5C**

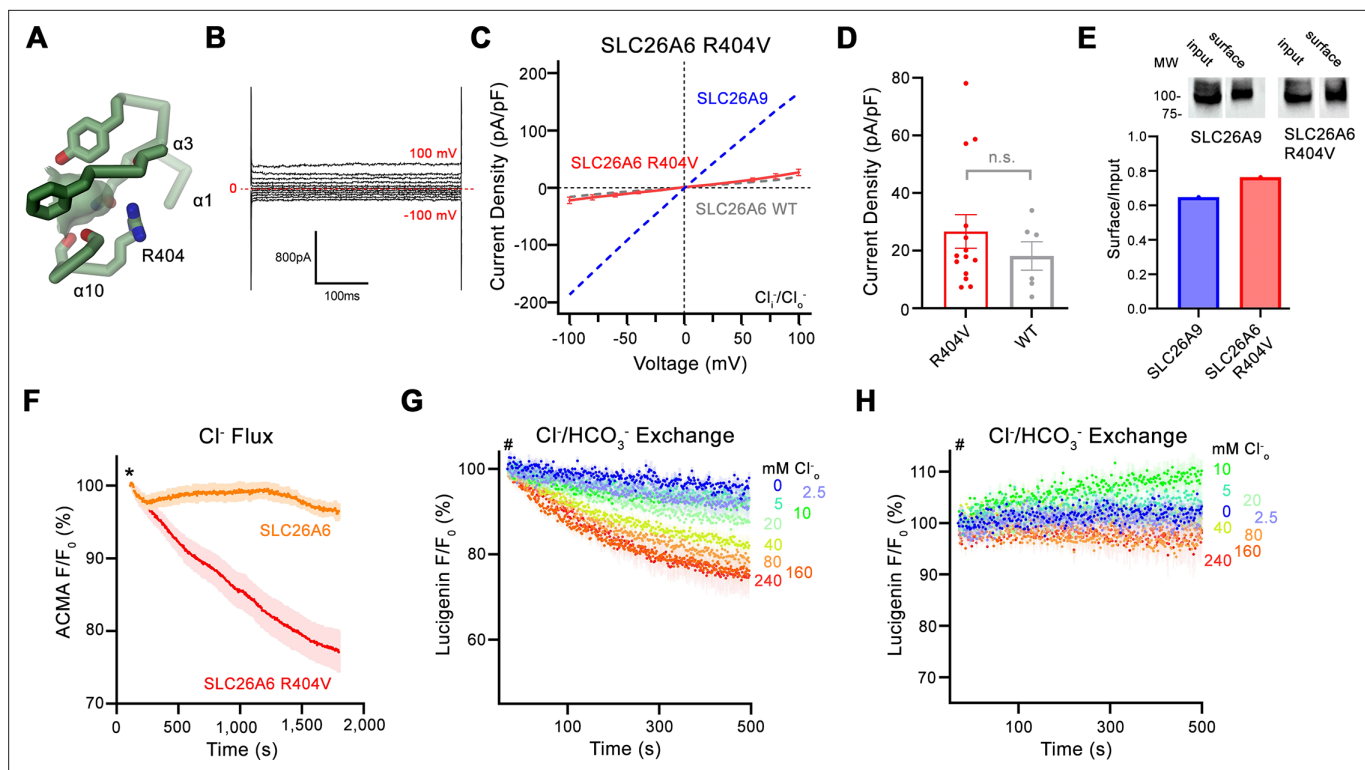


**Figure 5.** Functional properties of a structure based SLC26A6 construct. **(A)** SLC26 ion binding site showing surrounding residues including Arg 404. **(B)** Representative current trace and **(C)** current-voltage relationships of HEK 293 cells expressing the SLC26A6 mutant R404V. Data were recorded in the whole-cell configuration at symmetric (150 mM)  $\text{Cl}^-$  concentrations. Values show mean of 14 independent experiments. Dashed lines correspond to SLC26A9 (blue) and SLC26A6 data (grey) displayed in **Figure 1A and B**. **(D)** Average current densities of the SLC26A6 mutant R404V ( $n=14$ ) and SLC26A6 WT ( $n=6$ ). Values show currents recorded at 100 mV as displayed in **C** and **Figure 1B**. Although the currents were consistently larger for the mutant R404V, the difference is not statistically significant ( $p=0.69$ ). **(E)** Protein expression of SLC26A6 R404V and SLC26A9 at the surface of HEK cells determined by surface biotinylation. Ratio of biotinylated (right) over total protein (left) as quantified from a Western blot against myc-tag fused to the C-terminus of the respective constructs. **(F)** Uncoupled  $\text{Cl}^-$  transport mediated by SLC26A6 R404V reconstituted into proteoliposomes, as monitored by the fluorescence change of the pH gradient-sensitive fluorophore ACMA. Traces of SLC26A6 are shown for comparison. Data shows mean of five replicates from two independent reconstitutions for both constructs. **(G, H)** Coupled  $\text{Cl}^-/\text{HCO}_3^-$  exchange by the SLC26A6 mutant R404V monitored by the time- and concentration- dependent quenching of the fluorophore lucigenin trapped inside proteoliposomes. **(G)** Uncorrected traces and **(H)** traces corrected by the background obtained from empty liposomes displayed in **Figure 1—figure supplement 1D**, which do not show indication of transport. **(G, H)** Traces show mean of five independent experiments from two reconstitutions. **(C, D, F, G, H)** errors are s.e.m.

The online version of this article includes the following source data for figure 5:

**Source data 1.** Transport data and Western blot of the SLC26A6 mutant R404V.

**and D**), these currents are indicative for the capability of the mutant to mediate electrogenic  $\text{Cl}^-$  transport at low rates. We thus turned to our proteoliposome-based ACMA assay to confirm that side chain replacement has indeed conferred the ability to SLC26A6 to pass downhill  $\text{Cl}^-$  transport (**Figure 5F**). After demonstrating uncoupled chloride transport, we tested whether the mutant has retained its ability of mediating coupled  $\text{Cl}^-/\text{HCO}_3^-$  exchange using the fluorophore lucigenin but did not find pronounced  $\text{Cl}^-$  flux in this case (**Figure 5G and H**). Together our data suggest that the mutation of a conserved basic position in the ion binding site has compromised the ability of SLC26A6 to mediate coupled  $\text{Cl}^-/\text{HCO}_3^-$  exchange and instead facilitated uncoupled  $\text{Cl}^-$  transport with slow kinetics. While these findings underline the importance of Arg 404 for anion interactions and coupling, they also emphasize that the mutation of a single residue is insufficient to confer the complete functional phenotype of SLC26A9 as a fast uncoupled  $\text{Cl}^-$  conductor. Nevertheless, our results further underline the importance of the anion binding site in SLC26 transporters for the transport mechanism of its members.

## Discussion

By combining structural data obtained by cryo-EM with electrophysiology and transport assays, our study has elucidated the previously unknown architecture of SLC26A6, defined its transport properties and revealed the features that underlie the mechanistic distinction to the paralog SLC26A9. By using a novel  $\text{HCO}_3^-$  selective europium probe (Martínez-Crespo *et al.*, 2021), we have directly demonstrated the transport of this important physiological anion (Figure 1G). We have further clarified the controversy concerning the stoichiometry of anions transported by SLC26A6 (Ohana *et al.*, 2009). In the case of  $\text{Cl}^-/\text{HCO}_3^-$  transport, we detect a strict equimolar exchange of anions binding to a conserved site in the mobile core domain of the transmembrane transport unit (Figure 4B and H). Although not shown unambiguously, we assume an analogous mechanism also for  $\text{Cl}^-/\text{oxalate}$  exchange. Consequently, transport would be electroneutral in case of the monovalent  $\text{HCO}_3^-$  and electrogenic in case of the divalent oxalate (Figure 1E–H), which was already proposed in a previous study (Chernova *et al.*, 2005).

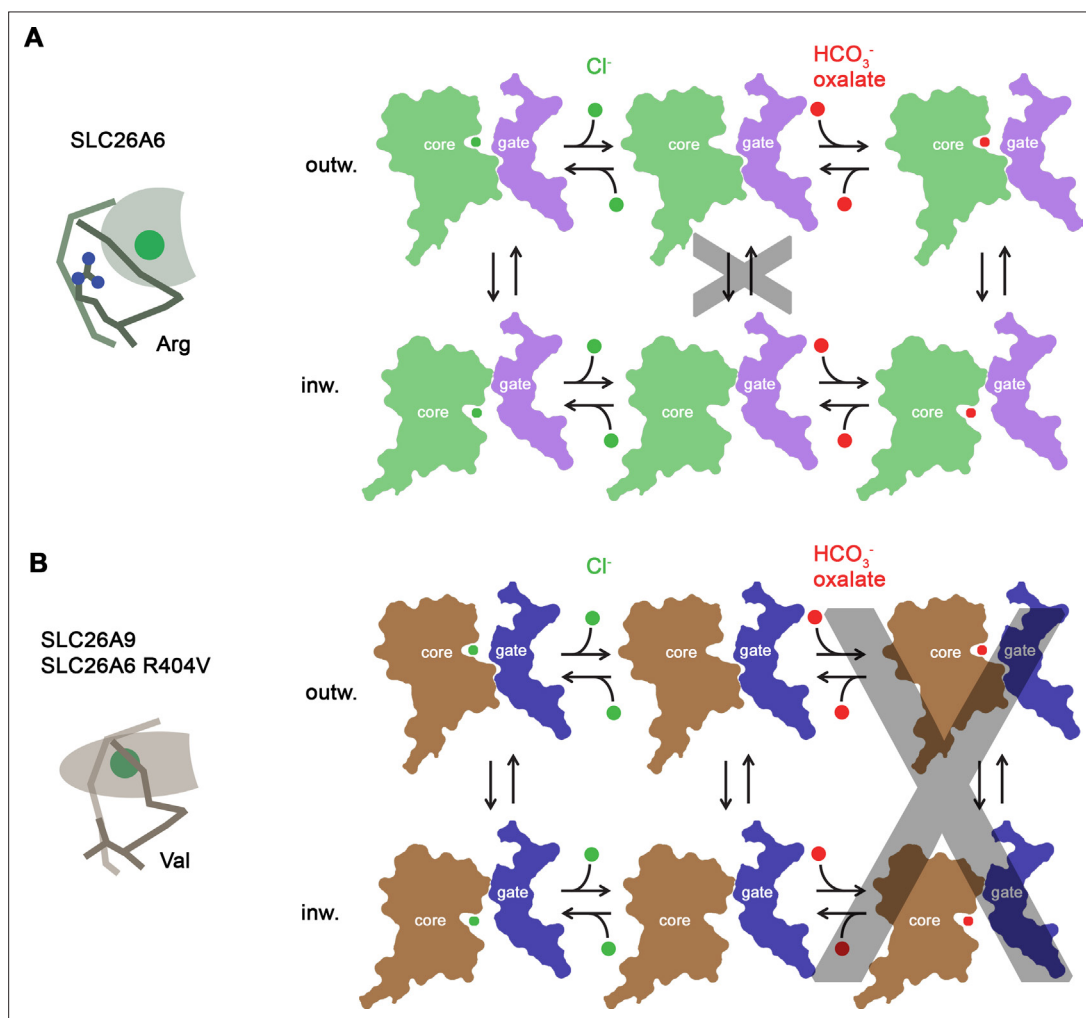


**Figure 6.** Transport mechanism. Features of the anion binding site (left) and kinetic schemes (right) of two SLC26 paralogs with distinct functional properties. **(A)** The coupled antiporter SLC26A6 mediates the strict stoichiometric exchange of  $\text{Cl}^-$  and  $\text{HCO}_3^-$  and presumably also of oxalate. The protein readily cycles between inward- and outward-facing conformations in substrate-loaded states, whereas the transition in an unloaded state is kinetically disfavored. The binding of different anions is facilitated by a large but shallow binding site with high field-strength. **(B)** The uncoupled  $\text{Cl}^-$  transporter SLC26A9 has a narrower substrate selectivity where both oxalate and  $\text{HCO}_3^-$  are not among the transported ions. Uncoupled  $\text{Cl}^-$  transport is likely mediated by a mechanism that allows the rapid transition of the unloaded transporter between inward- and outward-facing conformations. The transported ion binds to a site with low field-strength. A similar mechanism, although with slower kinetics, is mediated by a point mutant of SLC26A6 where a conserved Arg of the binding site is replaced by a Val, the corresponding residue found in SLC26A9.

Regarding their function, SLC26A6 and SLC26A9 show different features with respect to substrate selectivity and coupling (Ohana *et al.*, 2009). Remarkably, both proteins are capable of interacting with Cl<sup>-</sup> with similar mM affinity (Figure 1F; Walter *et al.*, 2019). However, they do this via distinct interactions in equivalent binding regions. In SLC26A9, Cl<sup>-</sup> binds in a deep pocket with low field strength, whereas the same pocket is shallower in SLC26A6, where a conserved arginine (Arg 404) increases the positive electrostatic potential and thus likely stabilizes the bound anion (Figure 4H, I and Figure 6). Together with the presence of additional residues at the binding site (i.e., Ser 401 at the N-terminal end of  $\alpha$ 10), the captured Cl<sup>-</sup> in SLC26A6 thus can rely on a larger density of polar interactions (Figure 4—figure supplement 1E,F). The same site likely also provides a suitable environment for HCO<sub>3</sub><sup>-</sup> and oxalate, neither of which are substrates of SLC26A9 (Figure 1A, Figure 1—figure supplement 1A,H; Dorwart *et al.*, 2007; Walter *et al.*, 2019). A similar anion interaction observed in SLC26A6 is also found in the paralogs SLC26A4 (Pendrin) (Liu *et al.*, 2023) and SLC26A5 (Prestin) (Futamata *et al.*, 2022; Ge *et al.*, 2021), which both share a similar substrate preference. The similarity between the core domains of SLC26A6 and Prestin is remarkable in light of the altered function of the latter, which is no longer capable of transporting ions and instead operates as motor protein in cochlear outer hair cells of mammals (Zheng *et al.*, 2000). While to some degree Prestin undergoes comparable conformational changes as other family members, as illustrated in the close relationship between occluded conformations of SLC26A9 and SLC26A5, the full transition into an outward-facing conformation to release the bound anion to the extracellular environment appears to be prohibited (Bavi *et al.*, 2021; Ge *et al.*, 2021).

Besides the absence of a residue carrying a positive charge, the altered binding site in SLC26A9 is also a consequence of concerted replacements of interacting amino acids on  $\alpha$ 1 and  $\alpha$ 10, which change the immediate environment of the bound ion and allow for a reorientation of the partly inserted helix  $\alpha$ 10 whose N-terminus contributes part of the interactions (Figure 4C and D). Collectively, these changes presumably lead to the altered ion selectivity. The importance of the described anion binding site for the transport mechanism is illustrated in the point mutation R404V in SLC26A6. The replacement of this basic residue, which was considered a hallmark in the distinction between SLC26A9 and other family members (Walter *et al.*, 2019), has compromised coupled Cl<sup>-</sup>/HCO<sub>3</sub><sup>-</sup> exchange and instead mediates uncoupled Cl<sup>-</sup> transport, although with considerably slower kinetics than in SLC26A9 (Figures 5B–G and 6).

From a mechanistic viewpoint SLC26A9 and SLC26A6 are distinguished by the sequence of conformations that together define the transport cycle (Figure 6). In the uncoupled SLC26A9, the transporter is able to transition between inward- and outward facing states at a high rate, which underlies the pronounced currents observed in patch clamp experiments (Figure 6B, Figure 1—figure supplement 1A). The same change of the access in an unloaded conformation is kinetically unfavorable in the coupled exchanger SLC26A6, as illustrated in the lack of current in electrophysiological recordings and the absence of a Cl<sup>-</sup> leak in a vesicle-based assay (Figures 1B–D, and 6A, Figure 1—figure supplement 1B). The basis for the distinctive kinetic features of both paralogs is currently still unclear, and we do at this stage not exclude the existence of a leaky channel-like conformation in SLC26A9. Such a conformation could potentially promote Cl<sup>-</sup> flow across a continuous aqueous pore without obligatory protein movement, although there is currently no structural evidence for its existence. The nature of the energy barrier, which prevents the shuttling of the unloaded state of SLC26A6 and other paralogs with similar functional phenotype (i.e. the transporters SLC26A1–4) has thus far remained elusive. It is likely that conformational changes are dictated by interactions between the mobile core domain with the immobile gate domain, which are both believed to operate as semi-independent entities (Geertsma *et al.*, 2015; Walter *et al.*, 2019). Remarkably, both units bury a similar contact area in the inward-facing conformations of SLC26A6 and SLC26A9 and do not exhibit pronounced differences in their interactions (Figure 3—figure supplement 1A,B). Additional contacts in SLC26A6 are established with the structured N-terminal part of the IVS region of the STAS domain of the interacting subunit, which appear to further stabilize the observed inward-facing conformation (Figure 2C). Similar interactions have also been found in the full-length transporter SLC26A9 (Chi *et al.*, 2020), which, next to the increased surface expression, could account for the strongly increased activity observed in the construct SLC26A9<sup>T</sup> where the IVS sequence of the protein was removed (Walter *et al.*, 2019). Besides the effect of the IVS, also the truncation of the C-terminus of SLC26A9 might have contributed to this high activity. The unstructured C-termini of family

members are weakly conserved and in case of SLC26A6 and SLC26A9, they contain a PDZ binding motif at their end, which is believed to tether either transporter to potential partners such as the anion channel CFTR via interacting scaffolding proteins (*Shcheynikov et al., 2006a*). In the isoform b of SLC26A9, a C-terminal extension was located in the aqueous cavity leading to the substrate binding site in the inward-facing conformation of SLC26A9, thereby locking the transporter in the observed conformation (*Chi et al., 2020; Figure 2—figure supplement 3A*). There is no similar extension found in any SLC26A6 isoforms, and the role of this interaction in a cellular environment is currently unclear, although it hints at a possible regulation in SLC26A9. Collectively, our study has provided novel insight into the structural basis of substrate selectivity and the mechanistic distinction between uncoupled and coupled transporters of the SLC26 family and thus provides a foundation for future investigations.

## Materials and methods

### Key resources table

Reagent type (species) or resource	Designation	Source or reference	Identifiers	Additional information
Chemical compound, drug	HyClone HyCell TransFx-H medium	Cytiva	SH30939.02	
Chemical compound, drug	1-palmitoyl-2-oleoyl-sn-glycero-3-phosphoethanolamine (POPE)	Avanti Polar Lipids	850757 C	
Chemical compound, drug	1-palmitoyl-2-oleoyl-sn-glycero-3-phospho-(1'-rac-glycerol) (POPG)	Avanti Polar Lipids	840457 C	
Chemical compound, drug	1-palmitoyl-2-oleoyl-glycero-3-phosphocholine (POPC)	Avanti Polar Lipids	850457 C	
Chemical compound, drug	Cholesterol	Sigma	C8667	
Chemical compound, drug	Triton X-100	Sigma	T9284	
Chemical compound, drug	Pepstatin A	Axon lab	A2205.0100	
Chemical compound, drug	Phenylmethylsulfonyl fluoride (PMSF)	Sigma	PMSF-RO	
Chemical compound, drug	Leupeptin	AppliChem	A2183,0100	
Chemical compound, drug	Benzamidine	Sigma	B6506	
Chemical compound, drug	Chloroform	Fluka	25690	
Chemical compound, drug	Glyco-diosgenin (GDN)	Anatrace	GDN101	
Chemical compound, drug	Diethyl ether	Sigma	296082	
Chemical compound, drug	DNase I	AppliChem	A3778	
Chemical compound, drug	Glycerin, Glycerol 86%	Roth	4043.3	
Chemical compound, drug	HCl	Merck Millipore	1.00319.1000	
Chemical compound, drug	HEPES	Sigma	H3375	
Chemical compound, drug	[Eu.L1] <sup>+</sup>	Loughborough University (Dr SJ Butler)	N/A	

Continued on next page



Continued

Reagent type (species) or resource	Designation	Source or reference	Identifiers	Additional information
Chemical compound, drug	ACMA	ThermoFischer Scientific	A1324	
Chemical compound, drug	CCCP	Sigma	C2759	
Chemical compound, drug	<i>N,N'</i> -Dimethyl-9,9'-biacridinium-dinitrat (Lucigenin)	Sigma	M8010	
Chemical compound, drug	Phosphate buffered saline	Sigma	D8537	
Chemical compound, drug	Strep-Tactin Superflow high capacity resin	IBA	2-1208-010	
Chemical compound, drug	D-desthiobiotin	Sigma	D1411	
Chemical compound, drug	Kolliphor P188	Sigma	K4894	
Chemical compound, drug	L-glutamine	Sigma	G7513	
Chemical compound, drug	Penicillin-streptomycin	Sigma	P0781	
Chemical compound, drug	Fetal bovine serum	Sigma	F7524	
Chemical compound, drug	Polyethylenimine 25 K MW, linear	Polysciences	23966-1	
Chemical compound, drug	40 kDa linear PEI MAX	Polysciences	24765-1	
Chemical compound, drug	Valproic acid	Sigma	P4543	
Chemical compound, drug	Calcium Chloride	Sigma	223506	
Chemical compound, drug	Magnesium Chloride	Fluka	63,065	
Chemical compound, drug	Potassium chloride	Sigma	746346	
Chemical compound, drug	Sodium chloride	Sigma	71380	
Chemical compound, drug	Terrific broth	Sigma	T9179	
Chemical compound, drug	Mouse-anti-myc primary antibody	Sigma	M4439	(WB 1:5000)
Chemical compound, drug	Peroxidase AffiniPure polyclonal Goat Anti-Mouse IgG (H+L)	Jackson ImmunoResearch	115-035-003 RRID: <a href="https://eutils.ncbi.nlm.nih.gov/entrez/eutils/rrid.cgi?db=AB">AB_10015289</a>	(WB 1:10000)
Commercial assay or kit	4–20% Mini-PROTEAN TGX Precast Protein Gels, 15-well, 15 µl	BioRad Laboratories	4561096DC	
Commercial assay or kit	Amicon Ultra-4 Centrifugal Filters Ultracel 100 K, 4 ml	Merck Millipore	UFC810024	
Commercial assay or kit	Borosilicate glass capillary with filament	Sutter Instrument	BF150-86-10HP	
Commercial assay or kit	0.22 µm Ultrafree-MC Centrifugal Filter	EMD Millipore	UFC30GV	

Continued on next page

Continued

Reagent type (species) or resource	Designation	Source or reference	Identifiers	Additional information
Commercial assay or kit	Biobeads SM-2 adsorbents	BioRad Laboratories	152–3920	
Commercial assay or kit	Avestin Extruder kit	Sigma	Z373400	
Commercial assay or kit	Pierce Cell Surface Biotinylation and Isolation Kit	ThermoFischer Scientific	A44390	
Commercial assay or kit	Amersham ECL Prime Western Blotting Detection Reagent	Cytiva	RPN2232	
Commercial assay or kit	Polycarbonate Membranes 400 nm	Sigma	610007	
Commercial assay or kit	Polycarbonate Membranes 50 nm	Sigma	610003	
Commercial assay or kit	96-well black walled microplates	ThermoFischer Scientific	M33089	
Commercial assay or kit	384-well black microplate flat-bottom	Greiner	781076	
Commercial assay or kit	Quantifoil R1.2/1.3 Au 200 Mesh	Electron Microscopy Sciences	Q2100AR1.3	
Commercial assay or kit	Superose 6 10/300 GL	Cytiva	17517501	
Other	BioQuantum Energy Filter	Gatan	N/A	
Other	HPL6	Maximator	N/A	
Other	K3 Direct Detector	Gatan	N/A	
Other	Titan Krios G3i	ThermoFisher Scientific	N/A	
Other	Viber Fusion FX7 imaging system	Witec	N/A	
Other	TECAN M1000 Infinite	TECAN	N/A	
Other	TECAN SPARK	TECAN	N/A	
Other	Vitrobot Mark IV	ThermoFisher Scientific	N/A	
Cell line (human)	HEK293S GnTi- & HEK293T	ATCC	CRL-3022 & CRL-1573	
Recombinant DNA reagent	Mammalian expression vector with C-terminal 3 C cleavage site, venus fluorescent tag, myc tag, SBP tag.	Dutzler laboratory	N/A	
Recombinant DNA reagent	<i>Mus musculus</i> SLC26A9 ORF shuttle clone	BioScience	GenBank BC160193	
Recombinant DNA reagent	<i>Homo sapiens</i> SLC26A6 cDNA clone	BioScience	GenBank BC017697	
Recombinant protein	HRV 3 C protease	Expressed (pET_3 C) and purified in Dutzler laboratory	N/A	RRID:SCR_016255 <a href="https://www.wyatt.com/products/software/astra.html">https://www.wyatt.com/products/software/astra.html</a>
Software, algorithm	ASTRA7.2	Wyatt Technology		RRID:SCR_015872 <a href="https://www.rbvi.ucsf.edu/chimerax/">https://www.rbvi.ucsf.edu/chimerax/</a>
Software, algorithm	ChimeraX 1.4	<b>Pettersen et al., 2021</b>		

Continued on next page

Continued

Reagent type (species) or resource	Designation	Source or reference	Identifiers	Additional information
Software, algorithm	Biorender	<a href="https://app.biorender.com/biorender-templates">https://app.biorender.com/biorender-templates</a>		
Software, algorithm	Coot v.0.9.4	<b>Emsley et al., 2010</b>	RRID:SCR_014222 <a href="https://www2.mrc-lmb.cam.ac.uk/personal/pemsley/coot/">https://www2.mrc-lmb.cam.ac.uk/personal/pemsley/coot/</a>	
Software, algorithm	cryoSPARC v3.2.0–4.0	Structura Biotechnology Inc.	RRID:SCR_016501 <a href="https://cryosparc.com/">https://cryosparc.com/</a>	
Software, algorithm	DINO		RRID:SCR_013497 <a href="http://www.dino3d.org">http://www.dino3d.org</a>	
Software, algorithm	EPU2.9	Thermo Fisher Scientific	N/A	
Software, algorithm	Phenix	<b>Liebschner et al., 2019</b>	RRID:SCR_014224 <a href="https://www.phenix-online.org/">https://www.phenix-online.org/</a>	
Software, algorithm	DeepEMhancer	<b>Sanchez-Garcia et al., 2021</b>	<a href="https://github.com/rsanchezgarc/deepEMhancer">https://github.com/rsanchezgarc/deepEMhancer</a>	
Software, algorithm	JALVIEW	<b>Waterhouse et al., 2009</b>		
Software, algorithm	Muscle	Edgar, 2004		
Software, algorithm	Axon Clampex 10.6	Molecular Devices	N/A	
Software, algorithm	Axon Clampfit 10.6	Molecular Devices	N/A	
Software, algorithm	Prism 9	GraphPad	N/A	
Strain, strain background (E Coli)	<i>E. coli</i> MC1061	Thermo Fisher Scientific	C66303	

## Construct generation

The open reading frame of human SLC26A6 (isoform 3, GenBank accession number: [BC017697](#)) and mouse SLC26A9 (GenBank accession number: [BC160193](#)) was amplified from a cDNA clone (Source BioScience) and cloned into into a pcDNA 3.1 vector (Invitrogen) modified to be compatible with the FX-cloning (**Geertsma and Dutzler, 2011**). The truncated murine SLC26A9 construct (SLC26A9<sup>T</sup>) was generated as previously detailed (**Walter et al., 2019**). All FX-modified expression constructs contained a C-terminal C3 protease cleavage site, venus YFP, myc-tag and streptavidin-binding protein (SBP). As a consequence of FX cloning, expressed constructs include an additional serine at the N-terminus and an alanine at the C-terminus. Following C3-cleavage, SLC26A6 carries a seven residues long C-terminal extension (of sequence ALEVL<sup>T</sup>FQ). For the generation of the hSLC26A6 point mutant R404V, the QuickChange (Aligent) mutagenesis method was used with the following primers: Forward: 5'-GCT CTA TGT CTG TGA GCC TGG TAC-3' and Reverse: 5'-GTA CCA GGC TCA CAG ACA TAG AGC-3'.

## Protein expression

Both HEK293S GnT1<sup>-</sup> (ATCC CRL-3022) and HEK293T (ATCC-1573) cell-lines used for protein expression tested negative for mycoplasma contamination.

Suspension HEK HEK293S GnT1<sup>-</sup> cells were grown and maintained in HyClone TransFx-H (GE Healthcare) media supplemented with 1% FBS, 1% Kolliphor P188, 100 U ml<sup>-1</sup> penicillin/streptomycin and 2 mM Glutamine. Cells were incubated at 37 °C and 5% CO<sub>2</sub> in TubeSpin Bioreactor 600 vessels (TPP) and shaken at 185 rpm.

For transient transfections, cells were split for transfection 24 hr prior from a cell density of 1–1.5 10<sup>6</sup> ml<sup>-1</sup>–0.4–0.6 10<sup>6</sup> ml<sup>-1</sup>. A ratio of 1.2 µg Plasmid DNA per 10<sup>6</sup> cells and 40 kDa linear PEI MAX (Polysciences) transfection reagent was used for protein expression. On the day of transfection, a 10 µg ml<sup>-1</sup> DNA dilution was incubated in non-supplemented DMEM media (Sigma). Linear PEI MAX was incubated with DNA at a ratio of 1:3 (w/w) from a 1 mg ml<sup>-1</sup> stock. After a 15 min incubation, the

DNA-PEI mix was added to suspension cells and co-incubated with 3 mM valproic acid (VPA). Cells were harvested after 48 hr and flash-frozen in liquid N<sub>2</sub> prior to storage at -80 °C.

### Protein purification

For protein purification, all protocols were performed at 4 °C. Cell pellets were thawed and mixed with extraction buffer (25 mM HEPES, pH 7.4, 200 mM NaCl, 5% glycerol, 2 mM CaCl<sub>2</sub>, 2 mM MgCl<sub>2</sub>, 2% glycol-diosgenin (GDN), 1 mM benzamidine, 10 μM leupeptin, 1 μM pepstatin A, 100 μM PMSF). For lysis cells were incubated for 2 hr at 4 °C under gentle agitation prior to ultracentrifugation (85,000 g, 30 min, 4 °C) to remove insoluble material. Lysate was filtered (5 μm filter, Sartorius) prior to binding to Streptactin Superflow high-capacity resin (IBA Lifesciences) equilibrated in wash buffer (25 mM HEPES, pH 7.4, 200 mM NaCl, 5% glycerol, 0.02% GDN) for 2 hr.

After discarding the flow-through of clarified lysate through gravity flow, Streptactin resin was washed with 40 column volumes (CV) wash buffer and SBP-tagged protein was eluted using wash buffer supplemented with 10 mM desthiobiotin (Sigma). Eluate was concentrated to 500 μl using a 100 kDa MWCO concentrator (Amicon) pre-equilibrated in wash buffer. C-terminal purification and detection tags were cleaved by 3 C protease at a 2:1 protease:protein mass ratio. Prior to size-exclusion chromatography, samples were passed through a 0.22 μm filter (Millipore). Samples were injected on the Äkta prime plus chromatography system (Cytiva) and separated on a Superose 6 10/300 column (GE Healthcare) in SEC buffer (10 mM HEPES, pH 7.4, 200 mM NaCl, 0.02% GDN). Protein containing peak samples were collected and used for cryo-EM sample preparation at a 2 mg ml<sup>-1</sup> concentration or used immediately for liposome reconstitution.

### Surface biotinylation

Adherent HEK293T cells were transfected at 80% confluency were transfected with 10 μg of plasmid encoding SLC26A6 WT and R404V constructs fused with a C-terminal SBP-Myc-Venus tag per 10 cm culture dish.

Transfection was performed using PEI MAX at a DNA:PEI ratio of 1:4. The Pierce Cell Surface Biotinylation and Isolation Kit (Thermo Fisher) was used according to manufacturer's guidelines. Cells were washed with PBS from 10 ml culture per construct and biotinylated following 24 hr of expression using EZ-Link Sulfo-NHS-SS-Biotin. Quenching was then performed using 750 μl quenching buffer and cells were harvested. Following a PBS wash-step and centrifugation at 1000 g, cells were re-suspended and lysed in 200 μl extraction buffer (25 mM HEPES, pH 7.4, 200 mM NaCl, 5% glycerol, 2 mM CaCl<sub>2</sub>, 2 mM MgCl<sub>2</sub>, 2% GDN, 1 mM benzamidine, 10 μM leupeptin, 1 μM pepstatin A, 100 μM PMSF) by gentle agitation for 1 hr at 4 °C. Insoluble fractions were removed by centrifugation at 50,000 g for 30 min and supernatant was incubated with 200 μl Neutravidin agarose slurry pre-equilibrated in wash buffer (25 mM HEPES, pH 7.4, 200 mM NaCl, 5% glycerol, 0.02% GDN) for 1 hr at 4 °C. The resin was washed three times with 200 μl of wash buffer and surface-biotinylated proteins were eluted by incubation with 200 μl wash buffer containing 50 mM fresh DTT for 1 hr at 4 °C with gentle mixing of the sample. Twenty μl of input, flow-through and surface-eluted samples were separated by SDS-PAGE. Samples were then transferred to a PVDF membrane and analyzed by Western blot using a mouse-anti-myc primary antibody (Sigma) and HRP-coupled goat-anti-mouse secondary antibody (Jackson ImmunoResearch). Antibodies were diluted 1:10,000 in TBS-T with 5% skimmed milk. Chemoluminescence signal was developed using ECL prime reagent (Cytiva) and imaged using a Fusion FX7 imaging system (Vilber).

### Liposome reconstitution

For liposome reconstitutions using the [Eu.L1<sup>+</sup>] bicarbonate-selective probe, lipid preparation was performed on the same day as protein purification. POPC:Cholesterol lipids (7:3 w/w ratio, Avanti) were pooled in a round-bottom flask and initially dried under N<sub>2</sub> flow to form a lipid film. Lipids were further dried under vacuum for 1 hr prior to re-hydration with [Eu.L1<sup>+</sup>] buffer (50 μM [Eu.L1<sup>+</sup>], 200 mM NaCl, 5 mM HEPES, pH 7.4). The resulting suspension was gently sonicated and stirred for 2 hr to generate a homogeneous mixture. Ten freeze-thaw cycles were performed to generate multilamellar liposomes before extrusion 29 times through x2 polycarbonate 400 nm filters to give unilamellar liposomes.

For protein incorporation, 10  $\mu$ l aliquots of 10% Triton X-100 were added in order to destabilize liposomes and permit protein incorporation. After reaching a plateau of the light scattering measured at 540 nm, 4 additional aliquots of Triton X-100 were added. The number of additions required for destabilization did not vary between reconstitutions. After the formation of destabilized liposomes, purified SLC26A6 was added at a lipid-to-protein ratio (LPR) of 50:1. To counteract [Eu.L1<sup>+</sup>] probe leakage, an additional equimolar 50  $\mu$ M [Eu.L1<sup>+</sup>] was added. The subsequent mixture was gently rotated at RT for 20 min prior to the addition of 250 mg SM-2 Bio-Beads (Bio-Rad) per 5 ml of sample. The sample was then incubated for 30 min at RT prior to incubation at 4 °C. Bio-Bead additions were performed over a 3-day period every 24 hr. BioBeads were removed by gravity filtration and the sample was used immediately for assay measurements.

For liposome reconstitution for the Lucigenin and ACMA assays, a similar procedure was used with the following adjustments. POPE:POPG lipids (3:1 w/w) were first pooled in a round-bottom flask and washed with diethyl ether prior to drying under N<sub>2</sub> for 1.5 hr. Lipids were then resuspended to 20 mg/ml in 10 mM HEPES, 150 mM KCl prior to sonication to form a homogeneous mixture. After three freeze-thaw cycles, the sample was frozen in liquid N<sub>2</sub> and stored at -80 °C until further use. Purified SLC6A9<sup>T</sup> was incorporated utilizing the triton-destabilisation method previously detailed at a LPR of 80:1 (w/w). Both SLC26A6 wildtype and the R404V mutant were incorporated at a 50:1 (w/w) ratio. Successful incorporation was confirmed by SDS-PAGE gel quantification. For all reconstitution procedures, mock empty liposomes lacking any purified protein were generated using the same protocols.

### [Eu.L1<sup>+</sup>] bicarbonate transport assay

For all measurements of HCO<sub>3</sub><sup>-</sup> transport, buffers were degassed to remove atmospheric CO<sub>2</sub>. After Bio-Bead removal via gravity filtration, proteoliposomes were pelleted and the excess [Eu.L1<sup>+</sup>] probe (Martínez-Crespo *et al.*, 2021) was removed by two ultracentrifugation and resuspension steps in symmetric outside buffer (200 mM NaCl, 5 mM HEPES, pH 7.4). Where 50 mM external NaCl was required, liposomes were pelleted by ultracentrifugation and resuspended in symmetric internal buffer (50  $\mu$ M [Eu.L1<sup>+</sup>], 200 mM NaCl, 5 mM HEPES, pH 7.4). Liposomes were further subjected to five freeze-thaw cycles and extruded 29 times using 400 nm polycarbonate filters. Two ultracentrifugation and resuspension-wash steps in asymmetric external buffer (50 mM NaCl, 5 mM HEPES, pH 7.4) were performed before the final resuspension in asymmetric external buffer.

For measurements of electroneutral Cl<sup>-</sup>/HCO<sub>3</sub><sup>-</sup> exchange, 100  $\mu$ l of SLC26A6 proteoliposomes were added to a 96-well flat bottom black plate (Greiner). Prior to measurement, liposome samples were gently bubbled under N<sub>2</sub> for 2 min to remove atmospheric CO<sub>2</sub> and residual HCO<sub>3</sub><sup>-</sup> from samples. Following the recording of a baseline emission for 20 fluorometric excitation/emission cycles (lasting 0.5 s each) using a Tecan Infinite M1000 Pro microplate reader, 10 mM HCO<sub>3</sub><sup>-</sup> was added to the liposomes. Normalized [Eu.L1<sup>+</sup>] emission (excitation = 332, emission = 617) was determined following the lysis of liposomes by addition of 0.4% Triton X-100 after cycle 300. Time gating of the recorded emission was performed using a 150  $\mu$ s lag-time between excitation and signal integration with an overall 850  $\mu$ s integration time. HCO<sub>3</sub><sup>-</sup> transport was measured in the presence of both, a four-fold NaCl gradient (200 mM inside/50 mM outside) and symmetrical conditions (200 mM inside/200 mM outside).

### ACMA assay

To compare the uncoupled chloride conduction properties of SLC26A6 and SLC26A9, proteoliposomes were prepared with an internal buffer concentration of 50 mM Na<sub>2</sub>SO<sub>4</sub>, 10 mM HEPES, pH 7.4. Proteoliposomes were sonicated in 20  $\mu$ l aliquots to form unilamellar vesicles prior to dilution into 9-amino-6-chloro-2-methoxyacridine (ACMA) assay buffer (2  $\mu$ M ACMA, 75 mM NaCl, 10 mM HEPES, pH 7.4). 100  $\mu$ l aliquots were added to a 96-well plate and after a baseline measurement period for 13 excitation/emission cycles (0.5 s per cycle), the protonophore carbonyl cyanide 3-chlorophenylhydrazone (CCCP) was added to dissipate the membrane potential and permit transporter-mediated anion-movement. ACMA fluorescence (excitation = 412 nm and emission = 482 nm), as a determinant of Cl<sup>-</sup> transport mediated H<sup>+</sup> influx, was measured using the Tecan Infinite M1000 Pro Plate Reader over 495 s or using the Tecan Spark Plate reader over 1800 s. Data were normalized to the point of CCCP addition.



To measure electrogenic oxalate transport, the same protocol was applied with the following exception: SLC26A6 liposomes consisted of an internal concentration of 150 mM KCl, 10 mM HEPES, pH 7.4 and an external concentration of 9.4–150 mM oxalate, 10 mM HEPES, pH 7.4. A total of 40  $\mu$ l aliquots were added to a black 384-well plate (Greiner) and ACMA fluorescence was measured on a TECAN Spark Plate Reader over 1200 s.

### Lucigenin assay

For measurement of Cl<sup>-</sup> uptake as consequence of Cl<sup>-</sup>/HCO<sub>3</sub><sup>-</sup> exchange, the halide-sensitive lucigenin dye (400  $\mu$ M) was incorporated into proteoliposomes containing either SLC26A6, the mutant SLC26A6 R404V or mock liposomes (all with a POPE:POPG composition of 3:1 w/w) in lucigenin assay buffer (200 mM HCO<sub>3</sub><sup>-</sup>, 10 mM HEPES, pH 7.4). To permit fluorophore incorporation, liposomes were diluted in the above buffer and three freeze-thaw cycles were performed prior to extrusion (17 times) using 50 nm polycarbonate filters. Ultracentrifugation was performed twice and resuspension in lucigenin assay buffer was performed to remove excess exterior lucigenin. Forty  $\mu$ l aliquots were transferred to a black 384-well plate and after 20 cycles (0.2 s per cycle), 0–240 mM NaCl diluted in assay buffer was added. Quenching of lucigenin fluorescence (excitation = 430 nm, emission = 505 nm) was measured as a determinant of Cl<sup>-</sup> influx for 300 cycles prior to lysis by 0.4% Triton X-100. Data are normalized to the point of NaCl addition and corrected for signal observed under mock liposome conditions.

### Electrophysiology

For electrophysiology recordings, adherent HEK293T cells were maintained in DMEM (Gibco) media and incubated at 37 °C and 5% CO<sub>2</sub>. Media was supplemented with 10% FBS, 1 mM L-glutamine, 4.5 g l<sup>-1</sup> Glucose, 1 mM sodium pyruvate and 100 U ml<sup>-1</sup> penicillin/streptomycin (Sigma). Cells were transfected at between 40% and 60% confluency and split into 60x15 mm dishes (Corning) the day prior to transfection. 5  $\mu$ g plasmid DNA was added together with linear PEI (25 kDa) at a ratio of 1:2.5 (w/w) DNA to PEI for transfection. DNA and PEI were mixed in non-supplemented media, incubated at RT for 10 min and added dropwise to cells with 3 mM VPA. Venus-fused constructs of human SLC26A6 and mouse SLC26A9 were used for recordings to facilitate the detection of expression through fluorescence microscopy. Cells were recorded from between 16 and 30 hr post-transfection.

Patch pipettes were formed from pulled and polished borosilicate glass capillaries (OD = 1.5 mm, ID = 0.86 mm, Sutter). When backfilled with 150 mM CsCl, patch pipettes yielded a resistance of between 2–4 M $\Omega$ . For voltage-clamp experiments, currents were recorded with an Axopatch 200B amplifier and digitized using a Digidata 1440 A A/D converter. Signals were filtered at 5 kHz and sampled at 20 kHz prior to acquisition with Clampex 10.6 (Molecular Devices). A voltage step protocol using a holding potential of 0 mV for 0.2 s was performed prior to 20 mV incremental voltage steps. The voltage steps ranged from -100 mV to +100 mV before returning to 0 mV. Recorded cell capacitance upon break-in varied between 10–30 pF with series resistance <10 M $\Omega$ . Calculated liquid junction potentials (JPCalcW, Molecular Devices) never surpassed 5 mV.

For whole-cell patch-clamp experiments, the intracellular pipette solution consisted of 146 mM CsCl, 2 mM MgCl<sub>2</sub>, 5 mM EGTA, 10 mM HEPES, pH 7.4. Extracellular bath solutions consisted of either 146 mM CsCl, 2 mM MgCl<sub>2</sub>, 5 mM EGTA, 10 mM HEPES, pH 7.4 or 150 mM CsHCO<sub>3</sub>/150 mM Cs<sub>2</sub>Oxalate, 2 mM Mg(OAc)<sub>2</sub>, 5 mM EGTA, 10 mM HEPES with pH adjusted using either CsOH or methanesulfonate. The pH of HCO<sub>3</sub><sup>-</sup> was monitored to ensure that the production of CO<sub>2</sub> and the consequent decline of HCO<sub>3</sub><sup>-</sup> never exceeded 20%. All acquired electrophysiology data were analyzed using Clampfit 11.0.3 (Molecular Devices), Excel (Microsoft), and GraphPad Prism 9 (GraphPad).

### Cryo-EM data acquisition

To proceed with structure determination by cryo-EM, 2.5  $\mu$ l samples of GDN-purified SLC26A6 were applied to glow-discharged holey carbon grids (Quantifoil R1.2/1.3 Au 200 mesh) at a concentration of 2 mg ml<sup>-1</sup>. Blotting of the sample (3–6 s) was performed at 4 °C at a relative humidity of 75% and grids were flash-frozen in liquid propane-ethane mix with a Vitrobot Mark IV (Thermo Fisher Scientific). A total of 11,962 images from two combined datasets were collected on a 300 kV Titan Krios G3i using a 100  $\mu$ m objective aperture. Data were collected in super-resolution mode using a post-column quantum energy filter (Gatan) with a 20 eV slit and a K3 Gatan direct detector. Data were acquired using EPU 2.7 for dataset 1 and EPU 2.9 for dataset 2 with aberration-free image shift (AFIS)

and a defocus range of  $-0.8$  to  $-2.4$   $\mu\text{m}$ . The dataset was recorded using a pixel size of  $0.651$   $\text{\AA}/\text{pixel}$  ( $0.3225$   $\text{\AA}/\text{pixel}$  in super-resolution mode) with a total exposure time of  $1$  s ( $36$  individual frames) and a dose of  $1.696$   $\text{e}/\text{\AA}^2/\text{frame}$  for dataset 1 and  $1.85$   $\text{e}/\text{\AA}^2/\text{frame}$  for dataset 2. The total electron dose for the specimen was  $61$   $\text{e}/\text{\AA}^2$  for dataset 1 and  $67$   $\text{e}/\text{\AA}^2$  for dataset 2.

### Cryo-EM data processing

Cryo-EM data were processed using CryoSPARC v3.2.0–4.0 (Punjani *et al.*, 2017; Figure 2—figure supplement 1, Table 1). All movies were subjected to patch motion correction. Following patch CTF estimation, high quality micrographs were identified based on relative ice thickness, CTF resolution estimation and total full frame motion. 1,749,907 particles were picked following the generation of 2D templates for automated template picking. Subsequently, picked particles were binned  $2.4\times$  using a box-size of 360 pixels for 2D classification (pixel size  $1.56$   $\text{\AA}/\text{pixel}$ ). Following three rounds of 2D classification, classes were selected that displayed general structural features characteristic for the SLC26 family in various orientations. From this, 256,581 particles were used to generate a ‘good’ ab initio reconstruction and a portion of rejected particles (16,030 particles) were used to generate a ‘junk’ reconstruction. 967,713 selected particles from 2D classification were subjected to heterogeneous refinement using the selected good reconstruction as a ‘template’ and the junk reconstruction as a ‘decoy’. After several rounds of heterogeneous refinement, the selected 507,174 particles and associated heterogeneously refined map were subjected to multiple rounds of non-uniform refinement with imposed C2 symmetry. Following iterative rounds of non-uniform and local CTF refinement, a reconstruction at a nominal resolution of  $3.55$   $\text{\AA}$  was generated. These particles were then subjected to a four-class ab initio reconstruction for further sorting resulting in one good map composed of 173,834 particles. Particles were re-extracted with a bin-1 pixel size of  $0.651$   $\text{\AA}/\text{pixel}$  using a 432 pixel-sized box and subjected to non-uniform refinement prior to a final three-class ab initio reconstruction resulting in a single high-quality map comprised of 93,169 particles. Multiple rounds of non-uniform refinement and local CTF refinement were performed. Finally, the resultant reconstruction maps were sharpened with the DeepEMhancer tool using the HighRes deep-learning model (Sanchez-Garcia *et al.*, 2021). The quality of the map was analyzed with 3DFSC (Tan *et al.*, 2017) for FSC validation and local resolution estimation.

### Cryo-EM model building and refinement

Map interpretation was performed in Coot (Emsley and Cowtan, 2004; Emsley *et al.*, 2010) using a model of SLC26A6 obtained from the AlphaFold Protein Structure Database (Jumper *et al.*, 2021; Varadi *et al.*, 2022) as template. The quality of the map allowed for the unambiguous assignment of residues 28–49, 62–594, and 655–747. The model was iteratively improved by real space refinement in PHENIX (Afonine *et al.*, 2018; Liebschner *et al.*, 2019) maintaining NCS and secondary structure constraints throughout. Figures were generated using ChimeraX (Pettersen *et al.*, 2004; Pettersen *et al.*, 2021) and Dino (<http://www.dino3d.org>). Surfaces were generated with MSMS (Sanner *et al.*, 1996).

### Acknowledgements

We thank the Center for Microscopy and Image Analysis (ZMB) of the University of Zurich for the support and access to the electron microscopes and Anastasiia Sukalskaia, Elena Lehmann, Katarzyna Drozdzyk and Melanie Arndt for their help in cryo-EM data acquisition. All members of the Dutzler lab are acknowledged for their help at various stages of the project. Justin Walter is acknowledged for the cloning of initial constructs and advice in the SLC26 project. This research was supported by a grant from the Swiss National Science Foundation (No. 31003A\_163421) to RD. SJB acknowledges the Engineering and Physical Sciences Research Council (EPSRC) for funding [EP/S032339/1].

## Additional information

### Funding

Funder	Grant reference number	Author
Schweizerischer Nationalfonds zur Förderung der Wissenschaftlichen Forschung	31003A_163421	Raimund Dutzler
Engineering and Physical Sciences Research Council	EP/S032339/1	Stephen J Butler

The funders had no role in study design, data collection and interpretation, or the decision to submit the work for publication.

### Author contributions

David N Tippett, Conceptualization, Data curation, Formal analysis, Validation, Investigation, Visualization, Methodology, Writing – original draft, Writing – review and editing, Cloned, expressed and purified proteins, carried out electrophysiology and transport experiments, prepared samples for cryo-EM, processed cryo-EM data and built models; Colum Breen, Resources, Writing – review and editing, Synthesized probe used for HCO<sub>3</sub><sup>-</sup> transport experiments; Stephen J Butler, Resources, Writing – review and editing; Marta Sawicka, Data curation, Formal analysis, Supervision, Writing – review and editing, Assisted in cryo-EM data collection and processing; Raimund Dutzler, Conceptualization, Data curation, Formal analysis, Supervision, Funding acquisition, Validation, Visualization, Writing – original draft, Project administration, Writing – review and editing

### Author ORCIDs

Marta Sawicka  <http://orcid.org/0000-0003-4589-4290>

Raimund Dutzler  <http://orcid.org/0000-0002-2193-6129>

### Peer review material

Reviewer #1 (Public Review): <https://doi.org/10.7554/eLife.87178.3.sa1>

Reviewer #2 (Public Review): <https://doi.org/10.7554/eLife.87178.3.sa2>

Reviewer #3 (Public Review): <https://doi.org/10.7554/eLife.87178.3.sa3>

Author Response: <https://doi.org/10.7554/eLife.87178.3.sa4>

## Additional files

### Supplementary files

- Transparent reporting form

### Data availability

The cryo-EM density map of hSLC26A6 has been deposited in the Electron Microscopy Data Bank under ID code EMD-17085. The coordinates for the atomic model of hSLC26A6 have been deposited in the Protein Data Bank under ID code 8OPQ. Source data files have been provided for Figure 1, Figure 1-figure supplement 1, Figure 2-figure supplement 1 and Figure 5.

The following datasets were generated:

Author(s)	Year	Dataset title	Dataset URL	Database and Identifier
Tippett DN, Breen C, Butler SJ, Sawicka M, Dutzler R	2023	Structure of Human Solute Carrier 26 family member A6 (SLC26A6) anion transporter in an inward-facing state	<a href="https://www.rcsb.org/structure/8OPQ">https://www.rcsb.org/structure/8OPQ</a>	RCSB Protein Data Bank, 8OPQ

*Continued on next page*

Continued

Author(s)	Year	Dataset title	Dataset URL	Database and Identifier
Tippett DN, Breen C, Butler SJ, Sawicka M, Dutzler R	2023	Structure of Human Solute Carrier 26 family member A6 (SLC26A6) anion transporter in an inward-facing state	<a href="https://www.ebi.ac.uk/emdb/EMD-17085">https://www.ebi.ac.uk/emdb/EMD-17085</a>	Electron Microscopy Data Bank, EMD-17085

## References

- Afonine PV**, Poon BK, Read RJ, Sobolev OV, Terwilliger TC, Urzhumtsev A, Adams PD. 2018. Real-space refinement in PHENIX for Cryo-EM and crystallography. *Acta Crystallographica. Section D, Structural Biology* **74**:531–544. DOI: <https://doi.org/10.1107/S2059798318006551>, PMID: 29872004
- Alka K**, Casey JR. 2014. Bicarbonate transport in health and disease. *IUBMB Life* **66**:596–615. DOI: <https://doi.org/10.1002/iub.1315>, PMID: 25270914
- Alper SL**, Sharma AK. 2013. The Slc26 Gene family of anion transporters and channels. *Molecular Aspects of Medicine* **34**:494–515. DOI: <https://doi.org/10.1016/j.mam.2012.07.009>, PMID: 23506885
- Bavi N**, Clark MD, Contreras GF, Shen R, Reddy BG, Milewski W, Perozo E. 2021. The conformational cycle of Prestin underlies outer-hair cell Electromotility. *Nature* **600**:553–558. DOI: <https://doi.org/10.1038/s41586-021-04152-4>, PMID: 34695838
- Bertrand CA**, Mitra S, Mishra SK, Wang X, Zhao Y, Pilewski JM, Madden DR, Frizzell RA. 2017. The CFTR trafficking mutation F508Del inhibits the constitutive activity of Slc26A9. *American Journal of Physiology. Lung Cellular and Molecular Physiology* **312**:L912–L925. DOI: <https://doi.org/10.1152/ajplung.00178.2016>, PMID: 28360110
- Butan C**, Song Q, Bai JP, Tan WJT, Navaratnam D, Santos-Sacchi J. 2022. Single particle Cryo-EM structure of the outer hair cell motor protein Prestin. *Nature Communications* **13**:290. DOI: <https://doi.org/10.1038/s41467-021-27915-z>, PMID: 35022426
- Chernova MN**, Jiang L, Friedman DJ, Darman RB, Lohi H, Kere J, Vandorpe DH, Alper SL. 2005. Functional comparison of mouse Slc26A6 anion exchanger with human Slc26A6 polypeptide variants: differences in anion selectivity, regulation, and Electrogenicity. *The Journal of Biological Chemistry* **280**:8564–8580. DOI: <https://doi.org/10.1074/jbc.M411703200>, PMID: 15548529
- Chi X**, Jin X, Chen Y, Lu X, Tu X, Li X, Zhang Y, Lei J, Huang J, Huang Z, Zhou Q, Pan X. 2020. Structural insights into the gating mechanism of human Slc26A9 mediated by its C-terminal sequence. *Cell Discovery* **6**:55. DOI: <https://doi.org/10.1038/s41421-020-00193-7>
- Clark JS**, Vandorpe DH, Chernova MN, Heneghan JF, Stewart AK, Alper SL. 2008. Species differences in Cl<sup>-</sup> affinity and in Electrogenicity of Slc26A6-mediated oxalate/Cl<sup>-</sup> exchange correlate with the distinct human and mouse Susceptibilities to nephrolithiasis. *The Journal of Physiology* **586**:1291–1306. DOI: <https://doi.org/10.1113/jphysiol.2007.143222>, PMID: 18174209
- Dorwart MR**, Shcheynikov N, Wang Y, Stippec S, Muallem S. 2007. Slc26A9 is a Cl<sup>-</sup> channel regulated by the WNK Kinases. *The Journal of Physiology* **584**:333–345. DOI: <https://doi.org/10.1113/jphysiol.2007.135855>, PMID: 17673510
- Dorwart MR**, Shcheynikov N, Yang D, Muallem S. 2008. The solute carrier 26 family of proteins in epithelial ion transport. *Physiology* **23**:104–114. DOI: <https://doi.org/10.1152/physiol.00037.2007>, PMID: 18400693
- Drew D**, Boudker O. 2016. Shared molecular mechanisms of membrane transporters. *Annual Review of Biochemistry* **85**:543–572. DOI: <https://doi.org/10.1146/annurev-biochem-060815-014520>, PMID: 27023848
- Emsley P**, Cowtan K. 2004. Coot: model-building tools for molecular Graphics. *Acta Crystallographica. Section D, Biological Crystallography* **60**:2126–2132. DOI: <https://doi.org/10.1107/S0907444904019158>, PMID: 15572765
- Emsley P**, Lohkamp B, Scott WG, Cowtan K. 2010. Features and development of Coot. *Acta Crystallographica. Section D, Biological Crystallography* **66**:486–501. DOI: <https://doi.org/10.1107/S0907444910007493>, PMID: 20383002
- Futamata H**, Fukuda M, Umeda R, Yamashita K, Tomita A, Takahashi S, Shikakura T, Hayashi S, Kusakizako T, Nishizawa T, Homma K, Nureki O. 2022. Cryo-EM structures of Thermostabilized Prestin provide mechanistic insights underlying outer hair cell Electromotility. *Nature Communications* **13**:6208. DOI: <https://doi.org/10.1038/s41467-022-34017-x>
- Ge J**, Elferich J, Dehghani-Ghahnaviyeh S, Zhao Z, Meadows M, von Gersdorff H, Tajkhorshid E, Gouaux E. 2021. Molecular mechanism of Prestin Electromotive signal amplification. *Cell* **184**:4669–4679. DOI: <https://doi.org/10.1016/j.cell.2021.07.034>, PMID: 34390643
- Geertsma ER**, Dutzler R. 2011. A versatile and efficient high-throughput cloning tool for structural biology. *Biochemistry* **50**:3272–3278. DOI: <https://doi.org/10.1021/bi200178z>, PMID: 21410291
- Geertsma ER**, Chang YN, Shaik FR, Neldner Y, Pardon E, Steyaert J, Dutzler R. 2015. Structure of a Prokaryotic fumarate transporter reveals the architecture of the Slc26 family. *Nature Structural & Molecular Biology* **22**:803–808. DOI: <https://doi.org/10.1038/nsmb.3091>, PMID: 26367249

- Jiang Z**, Asplin JR, Evan AP, Rajendran VM, Velazquez H, Nottoli TP, Binder HJ, Aronson PS. 2006. Calcium oxalate Urolithiasis in mice lacking anion transporter Slc26A6. *Nature Genetics* **38**:474–478. DOI: <https://doi.org/10.1038/ng1762>, PMID: 16532010
- Jumper J**, Evans R, Pritzel A, Green T, Figurnov M, Ronneberger O, Tunyasuvunakool K, Bates R, Židek A, Potapenko A, Bridgland A, Meyer C, Kohl SAA, Ballard AJ, Cowie A, Romera-Paredes B, Nikolov S, Jain R, Adler J, Back T, et al. 2021. Highly accurate protein structure prediction with AlphaFold. *Nature* **596**:583–589. DOI: <https://doi.org/10.1038/s41586-021-03819-2>, PMID: 34265844
- Kim HJ**, Myers R, Sihm CR, Rafizadeh S, Zhang XD. 2013. Slc26A6 functions as an Electrogenic Cl<sup>-</sup>/Hco<sub>3</sub><sup>-</sup> exchanger in cardiac myocytes. *Cardiovascular Research* **100**:383–391. DOI: <https://doi.org/10.1093/cvr/cvt195>, PMID: 23933580
- Knauf F**, Yang CL, Thomson RB, Mentone SA, Giebisch G, Aronson PS. 2001. Identification of a chloride-Formate exchanger expressed on the brush border membrane of renal proximal tubule cells. *PNAS* **98**:9425–9430. DOI: <https://doi.org/10.1073/pnas.141241098>, PMID: 11459928
- Liebschner D**, Afonine PV, Baker ML, Bunkóczi G, Chen VB, Croll TI, Hintze B, Hung LW, Jain S, McCoy AJ, Moriarty NW, Oeffner RD, Poon BK, Prisant MG, Read RJ, Richardson JS, Richardson DC, Sammito MD, Sobolev OV, Stockwell DH, et al. 2019. Macromolecular structure determination using X-rays, neutrons and electrons: recent developments in Phenix. *Acta Crystallographica. Section D, Structural Biology* **75**:861–877. DOI: <https://doi.org/10.1107/S2059798319011471>, PMID: 31588918
- Liu Q**, Zhang X, Huang H, Chen Y, Wang F, Hao A, Zhan W, Mao Q, Hu Y, Han L, Sun Y, Zhang M, Liu Z, Li GL, Zhang W, Shu Y, Sun L, Chen Z. 2023. Asymmetric pendrin homodimer reveals its molecular mechanism as anion exchanger. *Nature Communications* **14**:3012. DOI: <https://doi.org/10.1038/s41467-023-38303-0>, PMID: 37230976
- Lohi H**, Kujala M, Kerkelä E, Saarialho-Kere U, Kestilä M, Kere J. 2000. Mapping of five new putative anion transporter genes in human and characterization of Slc26A6, a candidate Gene for Pancreatic anion exchanger. *Genomics* **70**:102–112. DOI: <https://doi.org/10.1006/geno.2000.6355>, PMID: 11087667
- Lu F**, Li S, Jiang Y, Jiang J, Fan H, Lu G, Deng D, Dang S, Zhang X, Wang J, Yan N. 2011. Structure and mechanism of the Uracil transporter Uraa. *Nature* **472**:243–246. DOI: <https://doi.org/10.1038/nature09885>, PMID: 21423164
- Martínez-Crespo L**, Hewitt SH, De Simone NA, Šindelář V, Davis AP, Butler S, Valkenier H. 2021. Transmembrane transport of bicarbonate Unravelling. *Chemistry* **27**:7320. DOI: <https://doi.org/10.1002/chem.202101345>, PMID: 33956385
- Ohana E**, Yang D, Shcheynikov N, Muallem S. 2009. Diverse transport modes by the solute carrier 26 family of anion transporters. *The Journal of Physiology* **587**:2179–2185. DOI: <https://doi.org/10.1113/jphysiol.2008.164863>, PMID: 19015189
- Ohana E**, Shcheynikov N, Moe OW, Muallem S. 2013. Slc26A6 and Nadc-1 transporters interact to regulate oxalate and citrate homeostasis. *Journal of the American Society of Nephrology* **24**:1617–1626. DOI: <https://doi.org/10.1681/ASN.2013010080>, PMID: 23833257
- Pettersen EF**, Goddard TD, Huang CC, Couch GS, Greenblatt DM, Meng EC, Ferrin TE. 2004. UCSF Chimera—a visualization system for exploratory research and analysis. *Journal of Computational Chemistry* **25**:1605–1612. DOI: <https://doi.org/10.1002/jcc.20084>, PMID: 15264254
- Pettersen EF**, Goddard TD, Huang CC, Meng EC, Couch GS, Croll TI, Morris JH, Ferrin TE. 2021. UCSF ChimeraX: structure visualization for researchers, educators, and developers. *Protein Science* **30**:70–82. DOI: <https://doi.org/10.1002/pro.3943>, PMID: 32881101
- Punjani A**, Rubinstein JL, Fleet DJ, Brubaker MA. 2017. cryoSPARC: Algorithms for rapid Unsupervised Cryo-EM structure determination. *Nature Methods* **14**:290–296. DOI: <https://doi.org/10.1038/nmeth.4169>, PMID: 28165473
- Sanchez-Garcia R**, Gomez-Blanco J, Cuervo A, Carazo JM, Sorzano COS, Vargas J. 2021. Deepemhancer: a deep learning solution for Cryo-EM volume post-processing. *Communications Biology* **4**:874. DOI: <https://doi.org/10.1038/s42003-021-02399-1>, PMID: 34267316
- Sanner MF**, Olson AJ, Spehner JC. 1996. Reduced surface: an efficient way to compute molecular surfaces. *Biopolymers* **38**:305–320. DOI: [https://doi.org/10.1002/\(SICI\)1097-0282\(199603\)38:3%3C305::AID-BIP4%3E3.0.CO;2-Y](https://doi.org/10.1002/(SICI)1097-0282(199603)38:3%3C305::AID-BIP4%3E3.0.CO;2-Y), PMID: 8906967
- Shcheynikov N**, Ko SBH, Zeng W, Choi JY, Dorwart MR, Thomas PJ, Muallem S. 2006a. Regulatory interaction between CFTR and the Slc26 transporters. *Novartis Foundation Symposium* :177–186 PMID: 17120768.
- Shcheynikov N**, Wang Y, Park M, Ko SBH, Dorwart M, Naruse S, Thomas PJ, Muallem S. 2006b. Coupling modes and Stoichiometry of Cl<sup>-</sup>/Hco<sub>3</sub><sup>-</sup> exchange by Slc26A3 and Slc26A6. *The Journal of General Physiology* **127**:511–524. DOI: <https://doi.org/10.1085/jgp.200509392>, PMID: 16606687
- Smart OS**, Neduvellil JG, Wang X, Wallace BA, Sansom MS. 1996. HOLE: a program for the analysis of the pore dimensions of ion channel structural models. *Journal of Molecular Graphics* **14**:354–360. DOI: [https://doi.org/10.1016/s0263-7855\(97\)00009-x](https://doi.org/10.1016/s0263-7855(97)00009-x), PMID: 9195488
- Tan YZ**, Baldwin PR, Davis JH, Williamson JR, Potter CS, Carragher B, Lyumkis D. 2017. Addressing preferred specimen orientation in single-particle Cryo-EM through tilting. *Nature Methods* **14**:793–796. DOI: <https://doi.org/10.1038/nmeth.4347>, PMID: 28671674
- Varadi M**, Anyango S, Deshpande M, Nair S, Natassia C, Yordanova G, Yuan D, Stroe O, Wood G, Laydon A, Židek A, Green T, Tunyasuvunakool K, Petersen S, Jumper J, Clancy E, Green R, Vora A, Lutfi M, Figurnov M, et al. 2022. AlphaFold protein structure database: Massively expanding the structural coverage of protein-



- sequence space with high-accuracy models. *Nucleic Acids Research* **50**:D439–D444. DOI: <https://doi.org/10.1093/nar/gkab1061>, PMID: 34791371
- Walter JD**, Sawicka M, Dutzler R. 2019. Cryo-EM structures and functional characterization of murine Slc26A9 reveal mechanism of Uncoupled chloride transport. *eLife* **8**:e46986. DOI: <https://doi.org/10.7554/eLife.46986>, PMID: 31339488
- Wang Y**, Soyombo AA, Shcheynikov N, Zeng W, Dorwart M, Marino CR, Thomas PJ, Muallem S. 2006. Slc26A6 regulates CFTR activity in vivo to determine Pancreatic duct Hco3- secretion: relevance to cystic fibrosis. *The EMBO Journal* **25**:5049–5057. DOI: <https://doi.org/10.1038/sj.emboj.7601387>
- Wang C**, Sun B, Zhang X, Huang X, Zhang M, Guo H, Chen X, Huang F, Chen T, Mi H, Yu F, Liu L-N, Zhang P. 2019. Structural mechanism of the active bicarbonate transporter from Cyanobacteria. *Nature Plants* **5**:1184–1193. DOI: <https://doi.org/10.1038/s41477-019-0538-1>, PMID: 31712753
- Wang J**, Wang W, Wang H, Tuo B. 2020. Physiological and pathological functions of Slc26A6. *Frontiers in Medicine* **7**:618256. DOI: <https://doi.org/10.3389/fmed.2020.618256>
- Wang L**, Chen K, Zhou M. 2021. Structure and function of an *Arabidopsis thaliana* sulfate transporter. *Nature Communications* **12**:4455. DOI: <https://doi.org/10.1038/s41467-021-24778-2>
- Waterhouse AM**, Procter JB, Martin DMA, Clamp M, Barton GJ. 2009. Jalview version 2--A multiple sequence alignment editor and analysis workbench. *Bioinformatics* **25**:1189–1191. DOI: <https://doi.org/10.1093/bioinformatics/btp033>, PMID: 19151095
- Xie Q**, Welch R, Mercado A, Romero MF, Mount DB. 2002. Molecular characterization of the murine Slc26A6 anion exchanger: functional comparison with Slc26A1. *American Journal of Physiology. Renal Physiology* **283**:F826–F838. DOI: <https://doi.org/10.1152/ajprenal.00079.2002>, PMID: 12217875
- Zheng J**, Shen W, He DZZ, Long KB, Madison LD, Dallos P. 2000. Prestin is the motor protein of Cochlear outer hair cells. *Nature* **405**:149–155. DOI: <https://doi.org/10.1038/35012009>